nature metabolism

ARTICLES

https://doi.org/10.1038/s42255-020-00323-1

Space-time logic of liver gene expression at sub-lobular scale

Colas Droin[1,9], Jakob El Kholtei[2,9], Keren Bahar Halpern[3,9], Clémence Hurni[4], Milena Rozenberg[5], Sapir Muvkadi[6], Shalev Itzkovitz[7]✉ and Felix Naef[8]✉

The mammalian liver is a central hub for systemic metabolic homeostasis. Liver tissue is spatially structured, with hepatocytes operating in repeating lobules, and sub-lobule zones performing distinct functions. The liver is also subject to extensive temporal regulation, orchestrated by the interplay of the circadian clock, systemic signals and feeding rhythms. However, liver zonation has previously been analysed as a static phenomenon, and liver chronobiology has been analysed at tissue-level resolution. Here, we use single-cell RNA-seq to investigate the interplay between gene regulation in space and time. Using mixed-effect models of messenger RNA expression and smFISH validations, we find that many genes in the liver are both zonated and rhythmic, and most of them show multiplicative space-time effects. Such dually regulated genes cover not only key hepatic functions such as lipid, carbohydrate and amino acid metabolism, but also previously unassociated processes involving protein chaperones. Our data also suggest that rhythmic and localized expression of Wnt targets could be explained by rhythmically expressed Wnt ligands from non-parenchymal cells near the central vein. Core circadian clock genes are expressed in a non-zonated manner, indicating that the liver clock is robust to zonation. Together, our scRNA-seq analysis reveals how liver function is compartmentalized spatio-temporally at the sub-lobular scale.

The liver is a vital organ in maintaining body physiology and energy homeostasis. The liver carries out a broad range of functions related to carbohydrate and lipid metabolism, detoxification, bile-acid biosynthesis and transport, cholesterol processing, xenobiotic biotransformation and carrier-protein secretion. Notably, the liver performs catabolic and anabolic processing of lipids and amino acids, and produces the majority of plasma proteins[1]. Liver tissue is highly structured on the cellular scale, being heterogeneous in both cell-type composition and microenvironment[2]. In fact, liver tissue is made up of millions of repeating anatomical and functional subunits, called lobules, which in mice contain hepatocytes arranged in about 15 concentric layers with a diameter of about 0.5 mm (refs. [3,4]). On the portal side of the lobule, blood from the portal vein and the hepatic arteriole enters small capillaries called sinusoids and flows to the central vein. This is accompanied by gradients in oxygen concentration, nutrients and signalling along the portal–central axis, with the latter notably involving the Wnt pathway[5,6]. Due to this polarization, hepatocytes in different layers perform separate functions. This is accompanied by gradients of gene expression along the portal–central axis, with some genes expressed more strongly near the central vein, and vice versa for portally expressed genes. This phenomenon is termed liver zonation[1,7].

Recently, Halpern et al. combined single-cell RNA-sequencing (scRNA-seq) of dissociated hepatocytes and single-molecule RNA fluorescence in situ hybridization (smFISH) to reconstruct spatial mRNA expression profiles along the portal–central axis[8]. This analysis revealed an unexpected breadth of spatial heterogeneity, with ~50% of genes showing spatially non-uniform patterns. Among them, functions related to ammonia clearance, carbohydrate catabolic and anabolic processes, xenobiotic detoxification, bile-acid and cholesterol synthesis, fatty-acid metabolism, targets of the Wnt and Ras pathways and hypoxia-induced genes were strongly zonated.

Beyond its spatial heterogeneity, liver physiology is also highly temporally dynamic. Chronobiology studies have shown that temporally gated physiological and metabolic programmes in the liver result from the complex interplay among the endogenous circadian liver oscillator, rhythmic systemic signals and feeding–fasting cycles[9–11]. An intact circadian clock has repeatedly been demonstrated as key for healthy metabolism, also in humans[12]. In addition, the hepatocyte clock has specifically been shown to play a major role in the physiological coordination of nutritional signals and cell–cell communication (including non-hepatocytic cells) controlling rhythmic metabolism[13]. Temporal compartmentalization can prevent two opposite and incompatible processes from simultaneously occurring: for example, glucose is stored as glycogen following a meal and is later released into the blood circulation during the fasting period to maintain homeostasis in plasma glucose levels. Functional genomics studies of the circadian liver have typically been performed on bulk liver tissue[14]. In particular, several studies have shown how both the circadian clock and the feeding–fasting cycles pervasively drive rhythms of gene expression in bulk, impacting key sectors of liver physiology such as glucose homeostasis and lipid and steroid metabolism[15–18].

Here, we asked how these spatial and temporal regulatory programmes interact on the levels of individual genes and liver functions

[1]Institute of Bioengineering, School of Life Sciences, Ecole Polytechnique Fédérale de Lausanne, Lausanne, Switzerland. [2]Department of Molecular Cell Biology, Weizmann Institute of Science, Rehovot, Israel. [3]Department of Molecular Cell Biology, Weizmann Institute of Science, Rehovot, Israel. [4]Institute of Bioengineering, School of Life Sciences, Ecole Polytechnique Fédérale de Lausanne, Lausanne, Switzerland. [5]Department of Molecular Cell Biology, Weizmann Institute of Science, Rehovot, Israel. [6]Department of Molecular Cell Biology, Weizmann Institute of Science, Rehovot, Israel. [7]Department of Molecular Cell Biology, Weizmann Institute of Science, Rehovot, Israel. [8]Institute of Bioengineering, School of Life Sciences, Ecole Polytechnique Fédérale de Lausanne, Lausanne, Switzerland. [9]These authors contributed equally: Colas Droin, Jakob El Kholtei, Keren Bahar Halpern. ✉e-mail: shalev.itzkovitz@weizmann.ac.il; felix.naef@epfl.ch

more generally. In particular, can zonated gene expression patterns be temporally modulated on a 24-h time scale? And conversely, can rhythmic gene expression patterns observed in bulk samples exhibit sub-lobular structure? More complex situations may also be envisaged, such as time-dependent zonation patterns of mRNA expression (or, equivalently, zone-dependent rhythmic patterns), or sub-lobular oscillations that would escape detection on the bulk level due to cancelations. On the physiological level, it is of interest to establish how hepatic functions might be compartmentalized both in space and time. To study both the spatial and temporal axes, we performed scRNA-seq of hepatocytes at 4 different times in the 24-h day, extending a previous approach[8,19] to reconstruct spatial profiles at each time point. The resulting space-time patterns were statistically classified using a mixed-effect model describing both spatial and temporal variations in mRNA levels. In total, ~5,000 liver genes were classified on the basis of their spatio-temporal expression profiles, and a few representative profiles were further analysed with smFISH. Overall, this approach revealed the richness of space-time gene expression dynamics of the liver and provides a comprehensive view on how spatio-temporal compartmentalization is utilized at the sub-lobular scale in the mammalian liver.

Results

Single-cell RNA-seq captures space-time gene expression patterns in mouse liver. To investigate spatio-temporal gene expression patterns in mouse liver, we sequenced mRNA from individual liver cells obtained via perfusion from 10 ad libitum fed mice at 4 different times of the day (zeitgeber time (ZT) = 0 h, 6 h, 12 h and 18 h, 2–3 replicates per time point). The interval between ZT0 and ZT12 had the light on and corresponded to the fasting period in mice, while feeding happened predominantly between ZT12 and ZT0. We focused on hepatocytes by enrichment of cells according to size and in silico filtering, yielding a total of 19,663 cells (Methods). To validate that the obtained scRNA-seq data captured the expected variability in both spatial and temporal mRNA levels, we generated a clustering analysis of all cells by using a standard two-dimensional *t*-distributed stochastic neighbour embedding (*t*-SNE) dimensionality reduction (Methods) and coloured cells either by their positions along the central–portal axis (the a posteriori-assigned layers, see below) (Fig. 1a) or time (Fig. 1b). The clustering revealed that portally and centrally expressed landmark transcripts, such as *Cyp2f2* and *Cyp2e1*, encoding cytochrome P450 oxygenases involved in xenobiotic metabolism, marked cells in opposite regions of the projections (Fig. 1c,d). Likewise, time-of-day gene expression varied along an orthogonal direction (Fig. 1b), as shown for the fatty-acid elongase gene *Elovl3* peaking at ZT0 (Fig. 1e).

To obtain spatial mRNA expression profiles for each gene along the central–portal axis, we here introduced eight lobule layers, to which we assigned each individual cell. For this, we adapted a previous method that uses expression levels of landmark zonated genes to define a central–portal coordinate[19], with the modification that only landmark transcripts that were sufficiently expressed and that did not vary across mice and time points were used (27 central and 28 portal landmark genes, Methods). The resulting reconstructed (binned) mRNA expression profiles yielded 80 (8 layers over 10 mice) data points for each transcript. Although our resolution is lower compared with the typical 12–15 hepatocyte layers found in the liver[3,4], these reconstructions faithfully captured reference zonated genes, with both central, and portal, expression (Fig. 1f). Two examples of such genes are the centrally expressed glutamine synthethase (*Glul*), and the portally expressed urea cycle gene argininosuccinate synthetase (*Ass1*), showing mutually exclusive expression along the lobule[8]. The reconstruction also successfully identified transcripts of the core circadian clock, such as the master transcription factor gene *Bmal1* (also named *Arntl*), whose mRNA peaked between ZT18 and ZT0 (Fig. 1g)[20]. In addition to core clock genes, important clock outputs such as the PAR bZip transcription factor gene *Dbp*, which is a direct transcriptional target of BMAL1 regulating detoxification enzymes, peaked between ZT6 and ZT12 (Fig. 1g)[21]. Finally, genes showing both zonated and rhythmic mRNA accumulation were found (Fig. 1h), for example elongation of very long chain fatty acids 3 (*Elovl3*) is centrally expressed and peaks near ZT0, while phosphoenolpyruvate carboxykinase 1 (*Pck1*) regulating gluconeogenesis during fasting is expressed portally and peaks shortly before ZT12. Since most of the zonated profiles showed exponential shapes, and gene expression changes typically occur on a log scale[22], we log-transformed the data for further analysis (Methods, Fig. 1f and Extended Data Fig. 2a–c). Together, these examples indicate that the obtained gene expression profiles reliably capture spatial and temporal regulation of hepatocyte gene expression.

mRNA expression profiles categorized according to zonation and rhythmicity. To gain a systematic understanding of the space-time gene expression profiles, we next investigated if zonated gene expression patterns could be dynamic along the day, or conversely whether temporal expression patterns might be zone-dependent. To select a reliable set of reconstructed mRNA expression profiles for subsequent analyses, we filtered out genes with low expression, as well as genes with substantial biological variability across replicate liver samples, although this may be at the expense of a potentially decreased sensitivity (Methods). This yielded 5,058 spatio-temporal gene expression profiles (Extended Data Fig. 2d). An exploratory analysis of variance clearly identified zonated genes, rhythmic genes and fewer genes showing variability along both axes, with known zonated and rhythmic genes distributed as expected (Fig. 2a).

To identify possible dependencies between spatial and temporal variations, we built a mixed-effect linear model[23] for the space-time mRNA profiles, which extends harmonic regression to include a spatial covariate (Fig. 2b). In this model, rhythms are parameterized with cosine and sine functions, while spatial profiles are represented with (up to second-order) polynomials. In its most complex form, the model uses nine parameters describing spatially modulated oscillations, and one intercept per mouse (Methods). When some of the parameters are zero, the model reduces to simpler mRNA profiles, for example purely spatial or purely temporal expression profiles (Fig. 2c). We then used model selection[24] to identify the optimal parameterization and category for each gene (Methods). Finally, we classified each mRNA profile into one of five types of pattern (Fig. 2c). If only the intercept is used, the profile will be classified

Fig. 1 | An scRNA-seq approach to space-time gene expression in mouse liver. a–e, Global gene expression varies in both space and time, as shown using *t*-SNE visualizations of the scRNA-seq ($n = 19{,}663$ hepatocytes examined over 10 independent animals). Each dot represents one cell. Individual cells are coloured by the (a posteriori-assigned) lobule layer (**a**), ZT (**b**), expression levels of the zonated genes *Cyp2f2* and *Cyp2e1* (**c**,**d**) or the temporally regulated and centrally zonated gene *Elovl3* (**e**). **f–h**, Reconstructed spatial profiles (lobule layers 1–8) of selected zonated genes (**f**, top: *Glul* pericentrally (PC) expressed, bottom: *Ass1* periportally (PP) expressed); rhythmic but non-zonated genes (**g**, top: core clock gene *Bmal1* peaking at ZT18–ZT0, bottom: clock-controlled *Dbp*, peaking at ZT6–ZT12); zonated and rhythmic genes (**h**, top: *Elovl3*, bottom: *Pck1*). Expression levels correspond to fraction of total UMI per cell in linear scale. Log-transformed profiles are in Extended Data Fig. 1. Dots in **f–h** represent data points from the individual mice. Lines represent the mean expression per time point. Shaded areas represent one s.d. across the mice. For the scRNA-seq, we used $n = 2$ (ZT6, ZT18) or n = 3 mice (ZT0, ZT12) (Methods).

as flat or noisy (F/N, Methods). If only time-independent zonation parameters are retained, the predicted profile will be purely zonated (Z). If only layer-independent rhythmic parameters are retained, the predicted profile will be purely rhythmic (R). If only layer-independent rhythmic parameters and time-independent zonation parameters are retained, the profile is classified as

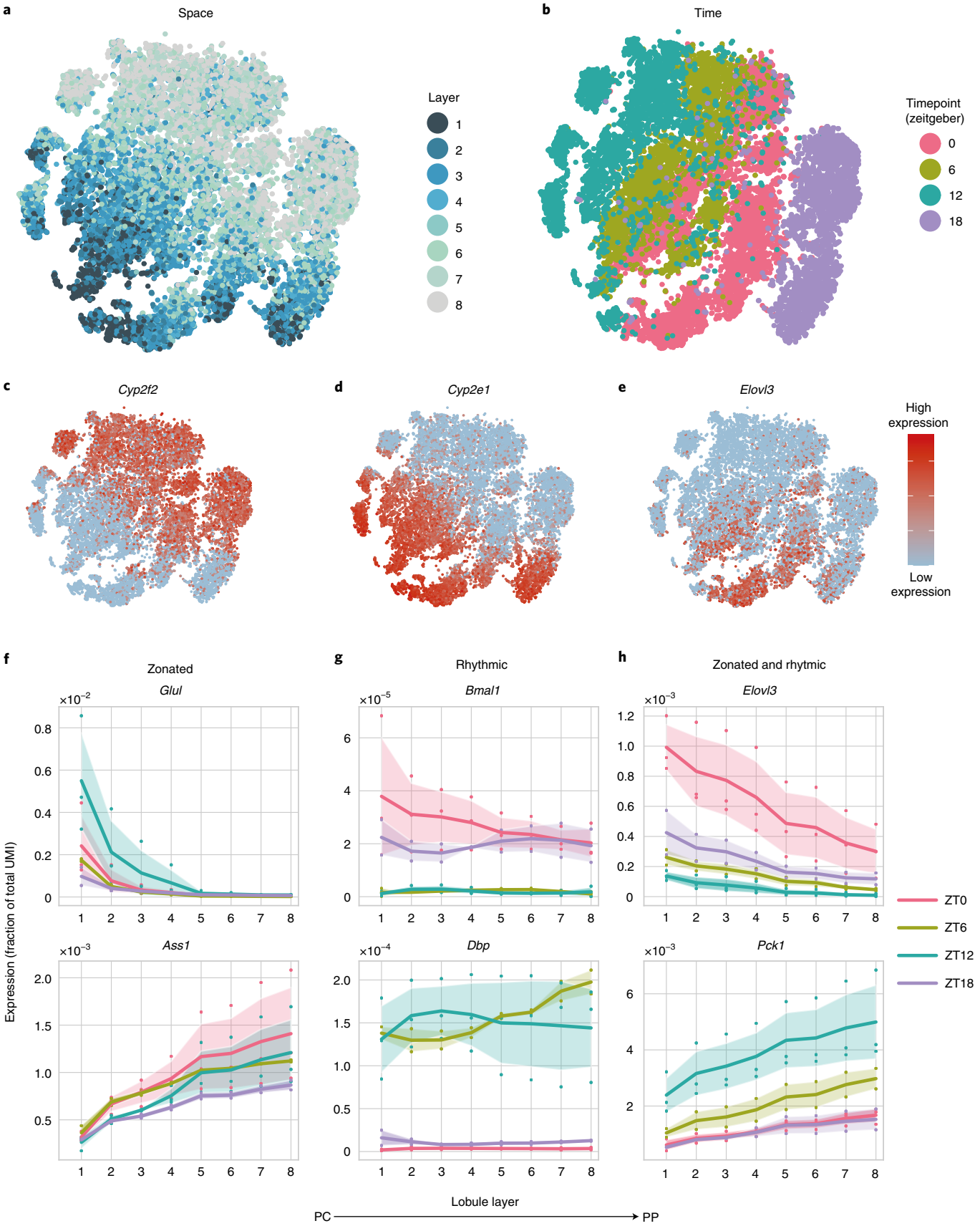

independent rhythmic-zonated (Z+R). If at least one layer-dependent rhythmic parameter is selected, the profile will be termed interacting (Z×R). This classification revealed that, overall, about 30% of the mRNA profiles were zonated (Z, Z+R and Z×R), and about 20% were rhythmic (R, Z+R and Z×R) (Fig. 2d). The peak times of these rhythmic transcripts were highly consistent with bulk chronobiology data[25] (Extended Data Fig. 2e). The entire analysis can be browsed as a web-app resource along with the corresponding data (https://czviz.epfl.ch).

Interestingly, we found that 7% of the analysed genes in the liver were both zonated and rhythmic. Such dually regulated transcripts represent 25% of all zonated transcripts, and 36% of all rhythmic transcripts, respectively. For example, the previously shown *Elovl3* transcript, encoding a protein involved in fatty-acid elongation, and *Pck1*, encoding a rate-limiting enzyme in gluconeogenesis, are prototypical Z+R genes (Fig. 1h and Extended Data Fig. 2c). Gluconeogenesis is an energetically demanding task[3]. As mice are in a metabolically fasted state requiring glucose production towards the end of the light phase (~ZT10) and oxygen needed for ATP production is most abundant portally[26], this process is indeed both spatially and temporally regulated. The dual regulation of zonated-rhythmic genes may therefore ensure optimal liver function under switching metabolic conditions.

Dually regulated genes were mostly Z+R, with only a minority of Z×R patterns. The average expression across categories showed that rhythmic genes are significantly less expressed on average than are genes in zonated categories, probably reflecting their shorter half-lives (Fig. 2e and Extended Data Fig. 2f). Surprisingly, we found few highly expressed flat genes. Together, our results show that mRNA expression of many zonated genes in hepatocytes is not static, and is in fact compartmentalized both in space and time.

Properties of dually zonated and rhythmic mRNA profiles. The majority of dually regulated genes are Z+R, which denotes additive (in log) space-time effects, or dynamic patterns in which slopes or shapes of spatial patterns do not change with time (Fig. 2c). On the other hand, interacting patterns (Z×R) are rare. Comparison of the proportions of central, mid-lobular (peaking in the middle of the portal–central axis) and portal genes among the purely zonated genes (Z), and independently zonated and rhythmic genes (Z+R), did not reveal significant differences (Fig. 3a), suggesting that rhythmicity is uncoupled with the direction of zonation. Similarly, comparing the phase distribution among the purely rhythmic genes (R) and the Z+R genes did not show a significant difference (Fig. 3b), indicating that zonation does not bias peak expression time. Moreover, oscillatory amplitudes were uncorrelated with the zonation slopes in Z+R genes (Fig. 3c). Finally, for Z×R genes with potentially more complex space-time patterns, we investigated the spreads in amplitudes and peak times across the layers (Fig. 3d). For wave-like patterns (phase modulated profiles), the phase difference across the lobule was up to 3 h, which corresponds to a difference in time between neighbouring hepatocytes on the order of 10 min for lobules of about 15 cell layers. On the other hand, amplitude-modulated patterns showed up to a twofold difference in oscillatory amplitude across the lobule.

To assess the potential physiological role of dually zonated and rhythmic transcripts, we asked if protein levels of the identified Z+R and Z×R genes accumulated rhythmically in a previous proteomics experiment[27]. In general, proteins rhythms are fewer, damped and time-delayed compared with mRNA rhythms due to protein half-lives[14,27,28] (see 'Discussion'). However, while R transcripts were twice more frequent than were Z+R transcripts, the proportions were inverted for rhythmic proteins. Indeed, we found that among 65 rhythmic proteins (with $q < 0.2$ in ref. [27]), 18 corresponded to Z+R and 10 to R transcripts. Moreover, the identified Z+R and Z×R genes with rhythmic protein accumulation cover key hepatic and zonated functions (Extended Data Fig. 3, for a functional interpretation, see below) and include rate-limiting enzymes. For example, for Z+R transcripts (Extended Data Fig. 3a), PCK1 (rate-limiting for gluconeogenesis), LPIN2 (*Lipin2*, encoding an enzyme that catalyses the conversion of phosphatidic acid to diacylglycerol during triglyceride, phosphatidylcholine and phosphatidylethanolamine biosynthesis), POR (cytochrome P450 oxidoreductase, required to activate P450 enzymes), DNAJA1 (HSP40 co-chaperone), ALAS1 (rate-limiting for haem biosynthesis), GNE (rate-limiting in the sialic acid biosynthetic pathway) and THRSP (biosynthesis of triglycerides from medium-length fatty-acid chains), show robust rhythms at the protein level. Similarly, for Z×R proteins, CYP7A1 (rate-limiting enzyme in bile-acid synthesis), CYP2A5 (coumarin 7-hydroxylase), SLC1A2 (high-affinity glutamate transporter) and multidrug-resistance protein ABCC2 show rhythms on the protein level (Extended Data Fig. 3b). Moreover, the protein rhythms accompanying those Z+R and Z×R transcripts peak with an expected delay of maximally about 6 h (ref. [28]) compared with the mRNA peak times (Extended Data Fig. 3c).

smFISH analysis of space-time mRNA counts. To substantiate the RNA-seq profiles, we performed smFISH experiments on a set of selected candidate genes with diverse spatio-temporal patterns. smFISH provides a sensitive and independent, albeit low-throughput, measurement of mRNA expression. Purely zonated genes (Z) have already been well studied with smFISH[8]. To analyse the core clock, we measured two genes peaking at different times, *Bmal1* and *Per1*, which were classified as R in the RNA-seq analysis. *Bmal1* (~ZT0) and *Per1* (~ZT12) phases were nearly identical in both experiments, and the rhythms did not depend on the lobular position consistent with R genes (Fig. 4a). We analysed three genes classified as Z+R: *Pck1* was indeed both portally biased and rhythmic in RNA-seq and smFISH (Fig. 4b); *Elovl3* was both centrally biased and rhythmic in RNA-seq and smFISH, even though the amplitude of the oscillations was damped on the portal

Fig. 2 | Space-time mRNA expression profiles categorized with mixed-effect models. a, Spatial and temporal variations for mRNA transcript profiles, calculated as s.d. of $\log_2$ expression along spatial or temporal dimensions. Coloured dots correspond to reference zonated genes (orange) and reference rhythmic genes (blue) (Methods). **b**, Extended harmonic regression model for spatio-temporal expression profiles describing a static but zonated layer-dependent mean $\mu(x)$, as well as layer-dependent harmonic coefficients ($a(x)$ and $b(x)$). All layer-dependent coefficients are modelled as second order polynomials; y is the log-transformed gene expression, x denotes the layer index, t denotes time, and i denotes the biological replicates. Temporal dependency is modelled with 24-h periodic harmonic functions. μ_i are random effects needed due to the data structure hierarchy (Methods). **c**, Schema illustrating the different categories of profiles. Depending on which coefficients are non-zero (Methods), genes are assigned to: F/N (not represented), Z, R, Z + R or Z×R. Graphs emphasize either zonation (top), with the x axis representing layers, or rhythmicity (bottom), with the x axis representing time (ZT). Right side of the panel: two examples of fits (*Elovl3* and *Cyp7a1*, respectively Z+R and Z×R). **d**, Number of transcripts in each category. **e**, Boxplot of the mean expression per category shows that zonated genes (Z, Z+R and Z×R) are more expressed than rhythmic (R) or flat/noisy (F/N). Z×R genes are the most expressed according to median expression (orange line). Box limits are lower and upper quartile, whiskers extend up to the first datum greater/lower than the upper/lower quartile plus 1.5 times the interquartile range. The number of genes per category is indicated. The remaining points are outliers. KW, Kruskal–Wallis test; MW for the Mann–Whitney (two-sided) test.

side in the FISH experiment (Extended Data Fig. 4a); and for *Arg1* (Arginase 1), the portal RNA-seq and smFISH profiles matched well (Extended Data Fig. 4b). Finally, *Acly* showed a pattern in smFISH data that validates its classification as Z × R, with a lower amplitude on the portal side, where the transcript is more highly expressed (Fig. 4c). Thus, overall, the reconstructed scRNA-seq and smFISH profiles were consistent, with minor discrepancies.

Space-time logic of hepatic functions. We next used our classification to explore the spatio-temporal dynamics of hepatic functions and signalling pathways in the liver. Given the prevalence of zonated gene expression profiles, we first analysed whether the circadian clock is sensitive to zonation. We found that profiles of reference core clock genes (Extended Data Fig. 5) were assigned to the rhythmic only category (R), except for *Cry1* and *Clock*, which were assigned

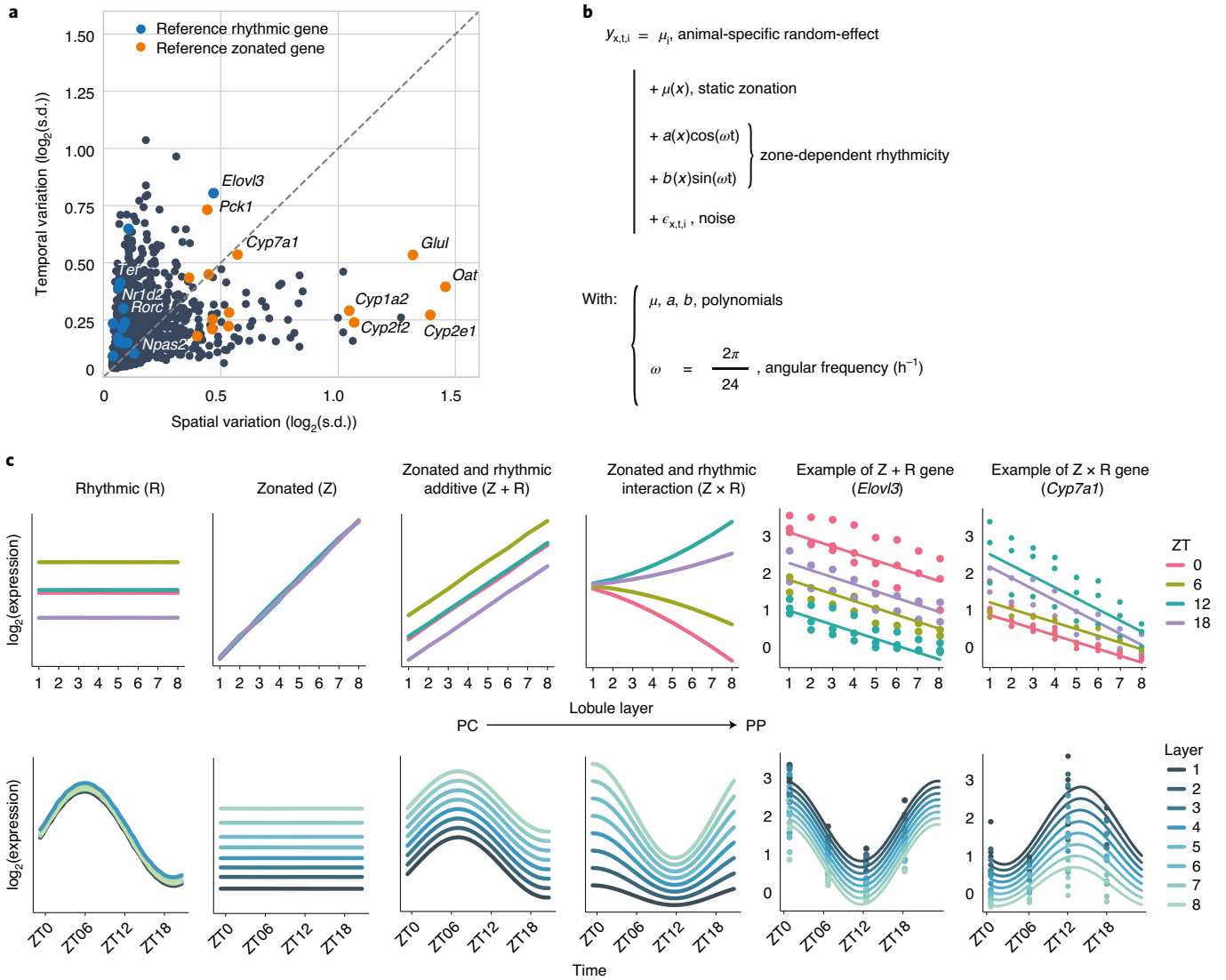

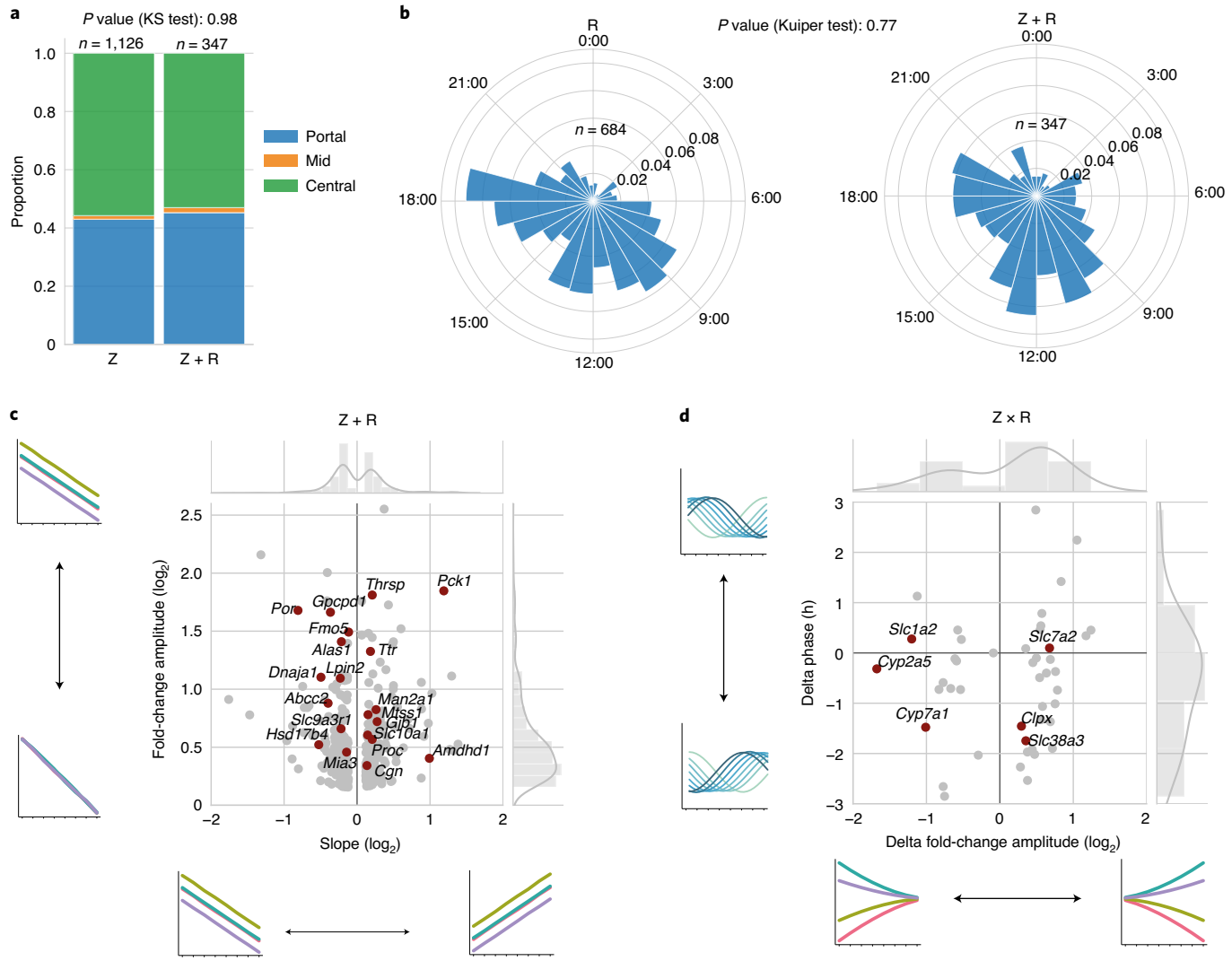

Fig. 3 | Properties of dually zonated and rhythmic mRNA profiles. a, Proportions of pericentral (green) and periportal (blue) transcripts are similar in Z and Z + R. Mid-lobular genes (orange) are rare (<2%). The number of genes are $n = 484$, 14, 628 and 157, 6, 184 for the portal, mid-lobular and central genes in Z and Z + R, respectively. KS, two-sided Kolmogorov–Smirnov test. **b**, Peak time distributions of rhythmic transcripts are similar in R and Z + R categories (two-sample Kuiper test). **c**,**d**, Effect sizes of zonation (slope) versus rhythmicity (fold-change amplitude, shown as $\log_2$(peak to trough)) in Z + R genes (**c**). Magnitude of time shifts (delta phase, in hours) versus fold-change amplitude gradient (delta amplitude, in $\log_2$) along the central–portal axis in Z × R genes (**d**). Genes for which the protein is also rhythmic ($P < 0.05$, harmonic regression, F test) in bulk data are indicated with dark red dots and labels (represented in Extended Data Fig. 3).

to Z + R, but with high probabilities also for R (Supplementary Table 2). This suggests that the circadian clock is largely non-zonated, as seen in the smFISH (Fig. 4a), and is therefore robust to the heterogenous hepatic microenvironment.

We then systematically explored enrichment of biological functions in the zonated category by querying the KEGG pathways database (Supplementary Table 3, Fig. 5 and Methods). In addition to recapitulating well-documented zonated liver functions[8,29], which we do not discuss here, this analysis highlighted Z and Z + R functions that, to our knowledge, had not been linked with liver zonation. For instance, we found that cytosolic chaperones accumulate centrally, while the endoplasmic reticulum (ER) chaperones linked with protein secretion accumulate portally (Fig. 5b,d and Extended Data Fig. 6). Both groups of chaperones peak during the activity/feeding phase, probably due to body temperature rhythms peaking during the active phase[30,31], and likely reflect increased needs of protein folding during times of high protein synthesis. Also, we found that mRNAs of ribosomal protein genes accumulate centrally (Z), as do proteasome components (Fig. 5a), which also contain rhythmic members (Z + R). In the liver, ribosomal proteins are rate-limiting for the synthesis of ribosomes, which themselves are rate-limiting for the synthesis of proteins[32]. Therefore, the overall protein synthesis rate is probably higher in these hepatocytes. Conversely, transcripts encoding components of the proteasome are involved in protein degradation. Together, these observations suggest that protein turnover is higher in centrally located hepatocytes, which are exposed to an environment with high concentrations of xenobiotics and hypoxic stress[33].

In addition, while many mitophagy genes are expressed centrally (Z), some of those also show robust temporal rhythms peaking during the fasting period (Z + R), in particular two gamma-aminobutyric acid receptor-associated proteins (encoded by *Gabarap* and *Gabarapl1*) with an important function in autophagosome-mediated autophagy[34]. Consistently with this

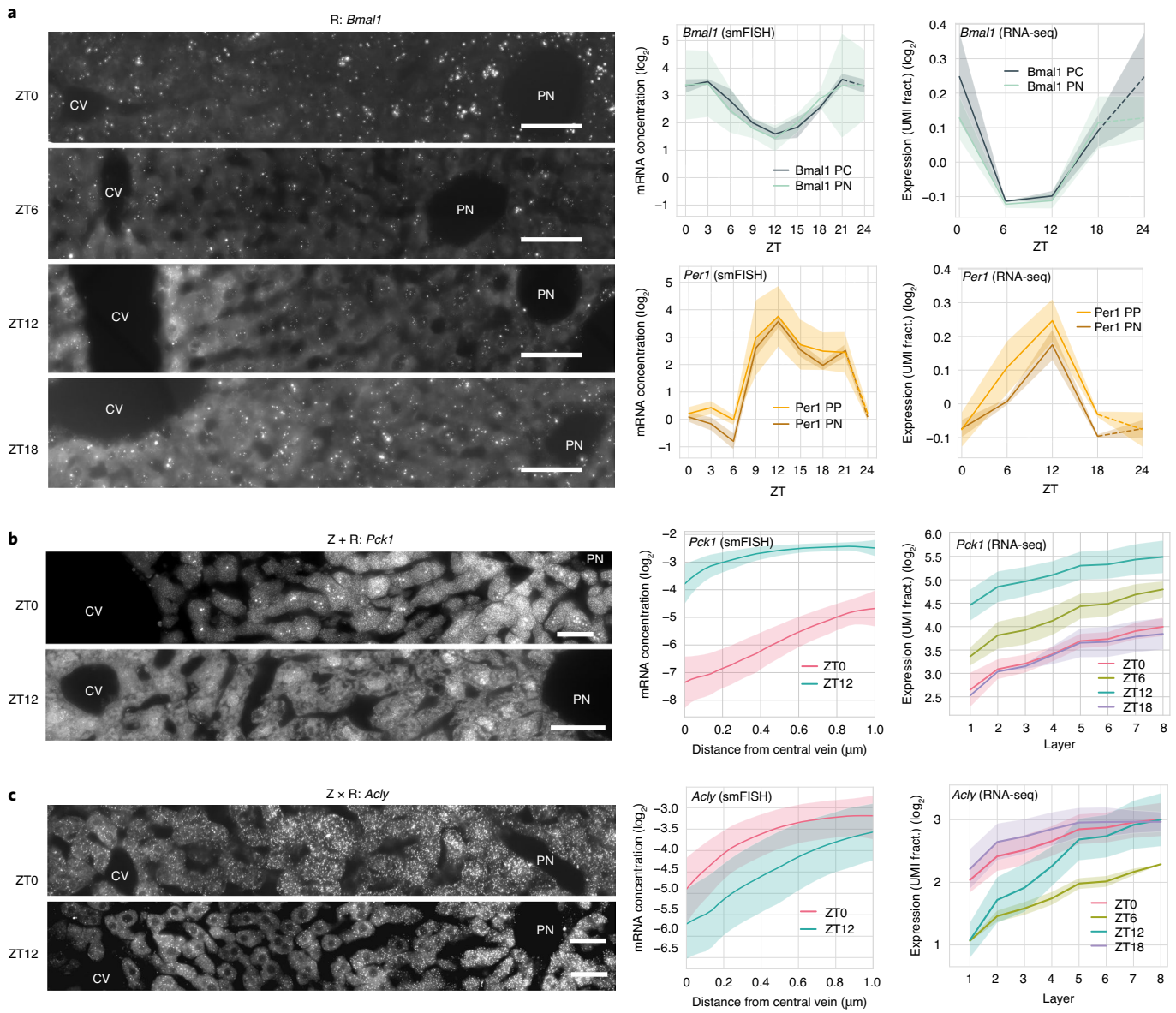

Fig. 4 | smFISH analysis of rhythmic and zonated transcripts. a, smFISH (RNAscope, Methods) of the core clock genes *Bmal1* and *Per1* (both assigned to R) in liver slices sampled every 3 h. Left, representative images at ZT0, ZT06, ZT12 and ZT18 for *Bmal1*. The central vein (CV) and a portal node (PN) are marked. Scale bar, 50 μm. Endothelial cells lining the PC and cholangiocytes surrounding the PP were excluded from the quantification. mRNA transcripts and nuclei were detected in PN and PC zones (Methods). Right, temporal profiles of *Bmal1* and *Per1* from smFISH at 8 time points from ZT0 to ZT21, every 3 h (the line shows the mean number of quantified mRNAs, shaded areas indicate s.d. across 5–8 images from 1 animal per time point), and scRNA-seq (same representation as in Fig. 1f–h, PC is layer 1, PN is layer 8), both in PN and PC regions. **b**,**c**, smFISH (Stellaris, Methods) for *Pck1* (Z + R) and *Acly* (Z × R) in liver slices sampled every 12 h. Left, representative images at ZT0 and ZT12 for *Pck1* (**b**) or *Acly* (**c**). The central vein and a portal node are marked. Scale bar, 20 μm. Right, quantified profiles for each gene at the two time points from smFISH (the line shows the mean number of quantified mRNAs, shaded areas indicate s.d. across at least ten independent images taken from at least two mice per time point) and scRNA-seq (same representation as in Fig. 1f–h). As above, the scRNA-seq used $n = 2$ (ZT6, ZT18) or $n = 3$ mice (ZT0, ZT12).

temporal regulation, we had previously reported that the nuclear abundance of the fasting-dependent regulators of autophagy TFEB and ZKSCAN3 peaked near ZT6 (ref. [35]). Moreover, the centrally and synchronously accumulating ubiquitin B mRNA (*Ubb*, Z + R) may contribute to triggering mitophagy[36]. Thus, centrally biased mitophagy may participate in removal of damaged mitochondria in the stressed central environment.

Similarly, genes involved in bile-acid synthesis and bile secretion are known to show zonated expression patterns[8] (Fig. 5c). Here, we found that while the rate-limiting enzyme in the bile-acid biosynthetic pathway, Cyp7a1 (Z × R, Fig. 2c), is known to be clock-controlled, with its mRNA[37,38] and protein[39] (Extended Data Fig. 7d) expressed maximally early during the feeding period, the ABC transporters sterolin-1 and 2 (ABCG5/ABCG8, both identified as Z + R), which excrete most of the biliary cholesterol[40], peak towards the end of the fasting period near ZT9.

Many detoxification enzymes of the cytochromes P450 (CYPs) superfamily are known to be centrally zonated in the liver[8], and several of those are found in the Z + R category. In particular, the flavin-containing monooxygenases FMO1, FMO2 and FMO5,

a

	Term	Adj. *P*	% central
Lipids	Cholesterol metabolism	5.58×10^{-11}	54
	Glycerophospholipid metabolism	1.61×10^{-3}	55
	Steroid biosynthesis	1.83×10^{-3}	57
	Fat digestion and absorption	3.15×10^{-3}	60
	Biosynthesis of unsaturated fatty acids	4.37×10^{-7}	78
	Fatty-acid elongation*	2.22×10^{-4}	80
	Steroid hormone biosynthesis	1.92×10^{-10}	82
	PPAR signalling pathway	6.87×10^{-9}	84
	Arachidonic acid metabolism	6.31×10^{-5}	90
	Peroxisome	2.24×10^{-13}	90
	Butanoate metabolism	1.14×10^{-4}	90
	Linoleic acid metabolism	5.49×10^{-6}	93
	Fatty-acid elongation	2.62×10^{-5}	93
Amino acids	Histidine metabolism	7.24×10^{-3}	0
	Arginine biosynthesis	3.84×10^{-5}	11
	Alanine, aspartate and glutamate metabolism	6.70×10^{-3}	22
	Phenylalanine, tyrosine and tryptophan biosynthesis	8.57×10^{-3}	25
	Phenylalanine metabolism	1.10×10^{-3}	25
	Glycine, serine and threonine metabolism	8.35×10^{-4}	27
	Cysteine and methionine metabolism	2.75×10^{-5}	40
	Tryptophan metabolism	9.63×10^{-8}	50
	β-Alanine metabolism	2.38×10^{-3}	66
	Valine, leucine and isoleucine degradation	2.24×10^{-7}	89
Protein homeostasis	Protein processing in endolasmic reticulum	1.41×10^{-5}	35
	Ribosome	1.41×10^{-9}	100
	Proteasome	1.67×10^{-4}	100
Carbohydrates	Pyruvate metabolism	5.26×10^{-4}	45
	Pentose and glucuronate interconversions	4.00×10^{-5}	75
Insulin	Glucagon signaling pathway	1.09×10^{-3}	26
Energy	AMPK signaling pathway	9.70×10^{-4}	27
	Oxidative phosphorylation	9.83×10^{-3}	30
	Citrate cycle (TCA cycle)	4.04×10^{-7}	42
	Nicotinate and nicotinamide metabolism	6.24×10^{-5}	50
	Glyoxylate and dicarboxylate metabolism	7.42×10^{-5}	54
	Synthesis and degradation of ketone of ketone bodies	4.22×10^{-3}	80
Autophagy	Mitophagy	9.74×10^{-3}	75
Vitamin	Ascorbate and aldarate metabolism	1.17×10^{-4}	80
	Retinol metabolism	7.56×10^{-9}	85
Heme	Porphyrin and chlorophyll metabolism	1.16×10^{-5}	78
Lysosome	Lysosome	1.80×10^{-3}	23
Bile	Bile secretion	6.15×10^{-7}	61
	Primary bile acid biosynthesis	6.00×10^{-4}	85
Detoxification	Drug metabolism	1.11×10^{-9}	78
	Glutathione metabolism	1.79×10^{-6}	78
	Metabolism of xenobiotics by cytochrome P450	5.98×10^{-7}	80
	Chemical carcinogenesis	3.99×10^{-11}	83
Iron	Ferroptosis	4.11×10^{-5}	30
Complements	Complement and coagulation cascades	4.76×10^{-16}	8

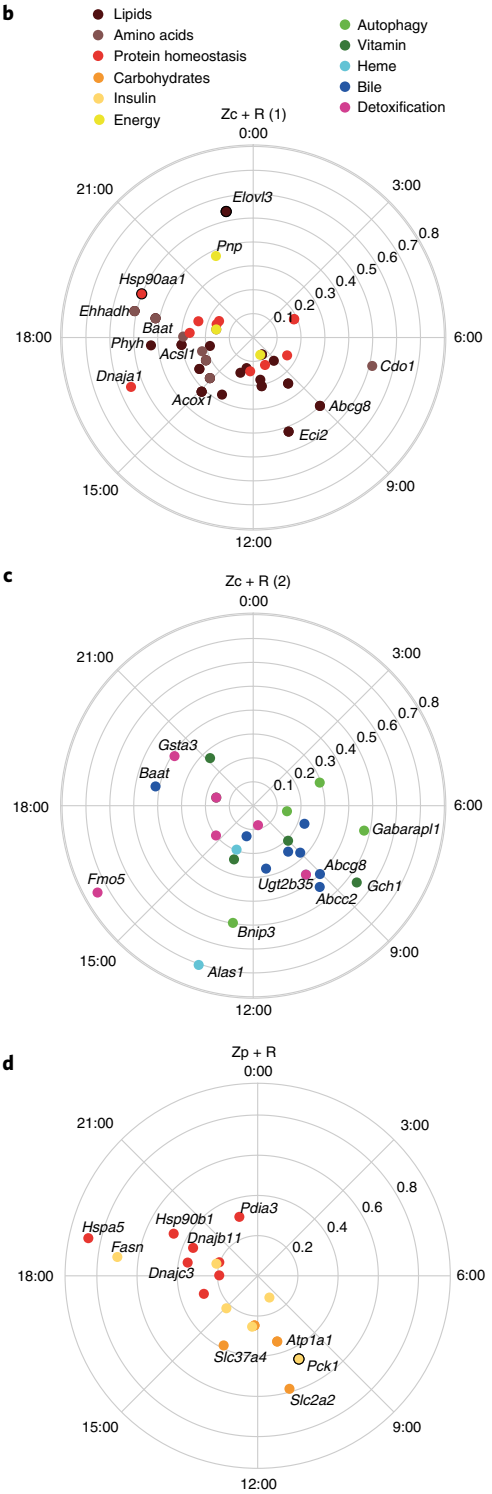

Fig. 5 | Space-time logic of compartmentalized hepatic functions for Z + R genes. a, KEGG analysis of the Z and Z + R genes. For clarity, only KEGG pathways (second column) with adjusted $P < 0.01$ (standard Enrichr[67] output test) are presented (Supplementary Table 3 for all enriched functions). The percentage of central genes is represented by a blue–red gradient. Terms labelled with asterisks appear central due to the KEGG annotation system; however, fatty-acid elongation is biased portally (see text). **b**–**d**, KEGG analysis of Z + R genes. Representations of genes in central (**b**,**c**) and portal (**d**) enriched Z + R categories (Supplementary Table 3). Polar representation, peak expression times are arranged clockwise (ZT0 on vertical position), and amplitudes ($\log_2$, values indicated on the radial axes) increase radially. The radius coordinate of genes with an amplitude of >0.9 is halved (indicated with a black circle around the coloured dot).

which are NADPH-dependent monooxygenases involved in drug and xenobiotic detoxification, exhibit Z + R mRNA patterns with peak near ZT16 (Fig. 5c). Also, the FMO5 protein accumulates rhythmically (Fig. 3c and Extended Data Fig. 3). Moreover, the rate-limiting enzyme ALAS1 that produces the P450 cofactor haem was found as a centrally zonated Z + R transcript with peak

mRNA at ZT13, also showing a robust rhythm in protein expression (Extended Data Fig. 3).

To substantiate the above finding on heat shock genes, we examined the space-time behaviour of temperature-regulated genes. To this end, we considered targets (bound in chromatin immunoprecipitation followed by sequencing) of the heat shock transcription factor HSF1 (Chip-Atlas[41], includes our own liver data[16]). This showed that several targets, known to peak during the active phase[30,31], are also zonated (Extended Data Fig. 6). Notably, the cytoplasmic *Hsp90aa1* (encoding Hsp90A chaperone) and its interactor *Dnaja1* (encoding HSP40), as well as the mitochondrial *Hspd1* (encoding HSP60 chaperone), are expressed centrally, where protein turnover is high. In contrast, genes encoding ER-located chaperones, including *Hspb1* (encoding Hsp90B) and its interactor *Pdia3*, as well as *Hspa5* (encoding HSP70) and *Dnajc3* and *Dnajb11* (encoding ER-resident DNAJ/HSP40), are expressed portally, consistent with their role in folding proteins in the secretory pathway (secretion is known to occur portally[29]). On the other hand, the analysis of cold-induced genes (that is, CIRBP and analogues, taken from ref. [42]) did not show zonated gene expression.

Finally, we note that among all KEGG pathways related to lipids, a majority show central enrichment (Fig. 5a and Supplementary Table 3). Inspection of the genes involved shows that this is due to the large number of genes related to peroxisomal β-oxidation, that is lipid catabolism, which are incidentally also listed in biosynthesis KEGG pathways (Supplementary Table 3). However, fatty-acid synthesis is biased portally, as supported by key portally expressed genes, such as *Fasn*, *Srebf1*, *Acly*, *Acaca*, *Elovl2* and *Elovl5*; this also is consistent with the fact that oxygen needed for mitochondrial β-oxidation is most abundant portally[26]. On the other hand, *Elovl3*, which is known to be transcriptionally controlled by the peroxisome regulator PPARα and atypically regulated among ELOV-family fatty-acid elongases[43] is expressed centrally.

Space-time logic of activity of signalling pathways. Signalling pathways that include Wnt, Ras and hypoxia have been shown to shape hepatocyte zonation[8]. We therefore examined the space-time activities of these pathways, extracted from the behaviour of canonical target genes. We mainly focused on Wnt, as it is often considered the master regulator of liver zonation[44]. To systematically investigate spatio-temporal WNT–β-Catenin activity in the liver, we extracted a set of Wnt targets derived from an adenomatous polyposis coli gene knockout (APC-KO) mouse liver[8,45]. We found that rhythmic transcripts (in the R, Z+R and Z×R categories) are enriched among targets of the Wnt pathway, showing a proportion that increases with the strength of the targets, with the strongest Wnt targets containing 80% of rhythmic transcripts (Extended Data Fig. 7a). Positive Wnt targets were pericentral[8] and peaked between ZT9 and ZT12, whereas negative Wnt targets were periportal[8] and peaked between ZT21 and ZT3 (Fig. 6a).

To obtain a temporal view of Wnt activity, we considered the top 50 Wnt pathway targets (according to the liver APC-KO data) in the liver and analysed the temporal profiles from high-temporal-resolution bulk liver mRNA and from our scRNA-seq binned in three different zones: central (layers 1–2), mid-lobular (layers 3–5) and portal (layers 6–8) (Fig. 6b,d and Extended Data Fig. 7b,c). This analysis confirmed that the peak times of rhythmic Wnt targets are preferentially between ZT9 and ZT12, and that the bulk and single-cell data are consistent with each other, despite of the lower temporal sampling of the scRNA-seq. Further evidence of rhythmic Wnt–β-catenin activity was provided by our previous proteomics data[35] showing that the potent Wnt effector TCF4 (encoded by the *Tcf7l2* gene) has rhythmic nuclear abundance in mouse liver, with a peak phase at ZT7.5 (Fig. 6c), and hence explains the accumulation of its mRNA targets a few hours later. Among the rhythmic genes detected in bulk RNA-seq, the five strongest Wnt targets were, in decreasing order: *Axin2*, *Glul*, *Slc1a2*, *Tuba8* and *Rnf43*, with the latter showing the largest amplitude (Fig. 6d). Aall but *Tuba8* peaked in the morning. Note that *Glul*, an important marker of central zonation and a canonical Wnt target (just like *Axin2* and *Rnf43*), was assigned to the Z category, but with second highest probability for Z×R (Supplementary Table 2), peaking at ZT12.

In addition to the mRNA rhythms, we found that several of the Z+R or Z×R Wnt targets showed clear rhythms in bulk proteomics with the characteristic phase delays. The strongest five targets with rhythmic proteins (Extended Data Fig. 7d) included the rate-limiting enzyme in the bile-acid biosynthetic pathway CYP7A1, the NADPH-dependent monooxygenases involved in drug and xenobiotic detoxification FMO5, the P450 detoxification enzymes coumarin 7-hydroxylase (encoded by *Cyp2a5*), which may protect mice from dietary coumarin-induced toxicity[46], the high-affinity glutamate transporter Slc1a2 (encoded by *Eaat2*) and the multidrug-resistance protein ABCC2. All these proteins showed high-amplitude protein rhythms peaking during the feeding phase between ZT12 and ZT18. Thus, Wnt transcription activity is clearly rhythmic in the liver, and this rhythm can propagate to protein expression.

We next asked whether the temporal oscillations in the expression of Wnt-activated genes might correlate with temporal oscillations in Wnt morphogens produced by pericentral non-parenchymal liver cells. To this end, we performed smFISH experiments and quantified the expression of the Wnt ligand gene *Wnt2* (ref. [5]) and of *Rspo3* (refs. [6,47]), a critical facilitator of Wnt signalling, as well as the Wnt antagonist gene *Dkk3* (ref. [19]) (Fig. 7a,b). We found that both *Wnt2* and *Rspo3* in liver non-parenchymal cells (NPCs) exhibit non-uniform expression around the clock, with significantly higher mRNA levels at ZT0 ($P=4\times10^{-5}$ for *Wnt2*, and $P=2\times10^{-8}$ for *Rspo3*, Kruskal–Wallis, Fig. 7b). Given various delays between mRNA accumulation of ligands and expression of the Wnt targets, this timing is compatible with the peak nuclear accumulation of the TCF4 (encoded by *Tcf7l2*) transcription factor observed at ZT7.5 (Fig. 6c) and with the peaks in Wnt-activated genes between ZT6 and ZT12 (Fig. 6a,b). Differences in *Dkk3* expression were not significant ($P=0.053$). Thus, production of Wnt morphogens by central non-parenchymal liver cells might underlie the observed rhythmic Wnt pathway activity.

Ras signalling and hypoxia are two additional pathways that have been implicated in shaping hepatocyte zonation[8]. In agreement with ref. [8], we found that the negative targets of Ras were enriched in central genes, whereas the positive Ras targets were enriched in portal genes (data not shown). The rhythmic targets (R and Z+R) of hypoxia showed a pattern of temporal compartmentalization similar to those of Wnt (Extended Data Fig. 7e): the negative targets were enriched around ZT0 (dark–light transition) and underrepresented around ZT14, while the positive targets were enriched around ZT10 and underrepresented around ZT3. Ras targets, positive or negative, did not exhibit temporal bias.

Discussion

Recent genome-wide analyses of zonated gene expression in mouse and human liver[8,48,49] uncovered a rich organization of liver functions in space at the sub-lobular scale, while chronobiology studies of bulk liver tissue revealed a complex landscape of rhythmic regulatory layers orchestrated by a circadian clock interacting with feeding–fasting cycles and systemic signals[35,50–52]. Here, we established how these two regulatory programmes combine to shape the daily space-time dynamics of gene expression patterns and physiology in adult liver by extending our previous scRNA-seq approach[8]. We found that the liver uses gene expression programmes with many genes that exhibit compartmentalization in both space and time.

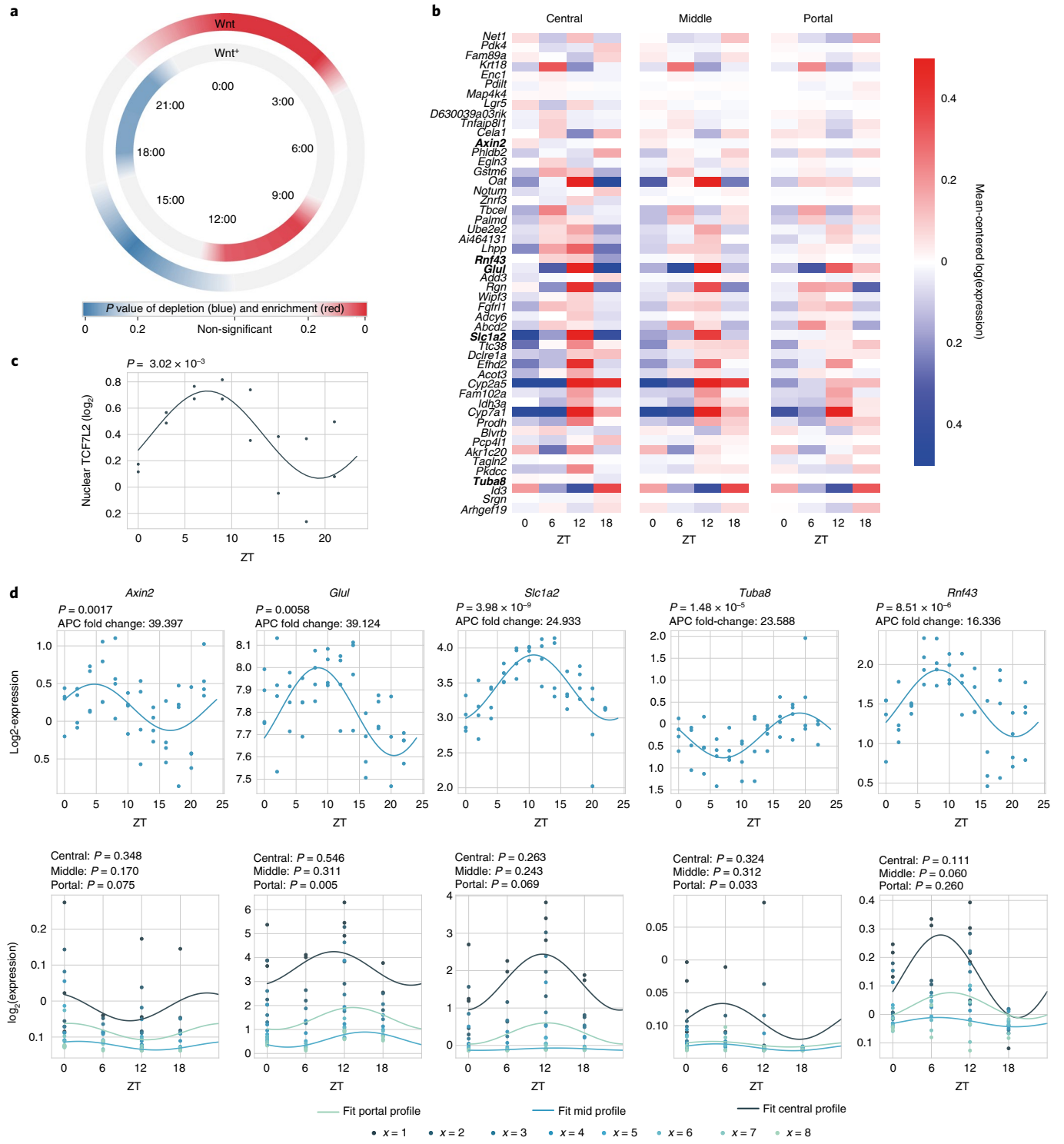

Fig. 6 | Rhythmic activity of Wnt signalling. a, Enrichment/depletion at different times (window size: 3 h), of both positive ($n = 471$) and negative ($n = 149$) Wnt targets (background: all R and Z + R genes). The colour map shows *P* values (two-tailed hypergeometric test): red indicates enrichment, and blue indicates depletion. **b**, Heatmaps representing scRNA-seq profiles of the top 50 Wnt targets (according to the APC-KO fold change, *Lgr5* was also added) showing rhythmic mRNA in bulk ($P < 0.01$, harmonic regression, *F* test, data from ref. [25]). The profiles are computed in three different zones of the central–portal axis: central (layers 1–2), mid-lobular (layers 3–5) and portal (layers 6–8). Gene profiles ($\log_2$) are mean-centred in each zone. An enrichment of the phases around ZT8–ZT14 can be observed, in agreement with Fig. 6a. mRNA expression profiles of the genes in bold are shown in **d**. **c**, Nuclear protein abundance from ref. [35] of the Wnt effector TCF4 (encoded by the *Tcf7l2* gene) in mouse liver shows a rhythm ($p = 0.003$, harmonic regression, $n = 2$, sampled every 3 h) peaking at ZT7.5, consistent with the accumulation of mRNA targets a few hours later (**a**). **d**, mRNA profiles from bulk RNA-seq (top) and scRNA-seq (bottom). Top five targets with the highest APC-KO fold change, and rhythmicity in the bulk data ($P < 0.01$, harmonic regression, *F* test, data from ref. [25]). Rhythmicity (indicated above each panel) is also computed in three different zones for the scRNA-seq data. As above, the scRNA-seq used $n = 2$ (ZT6, ZT18) or $n = 3$ mice (ZT0, ZT12).

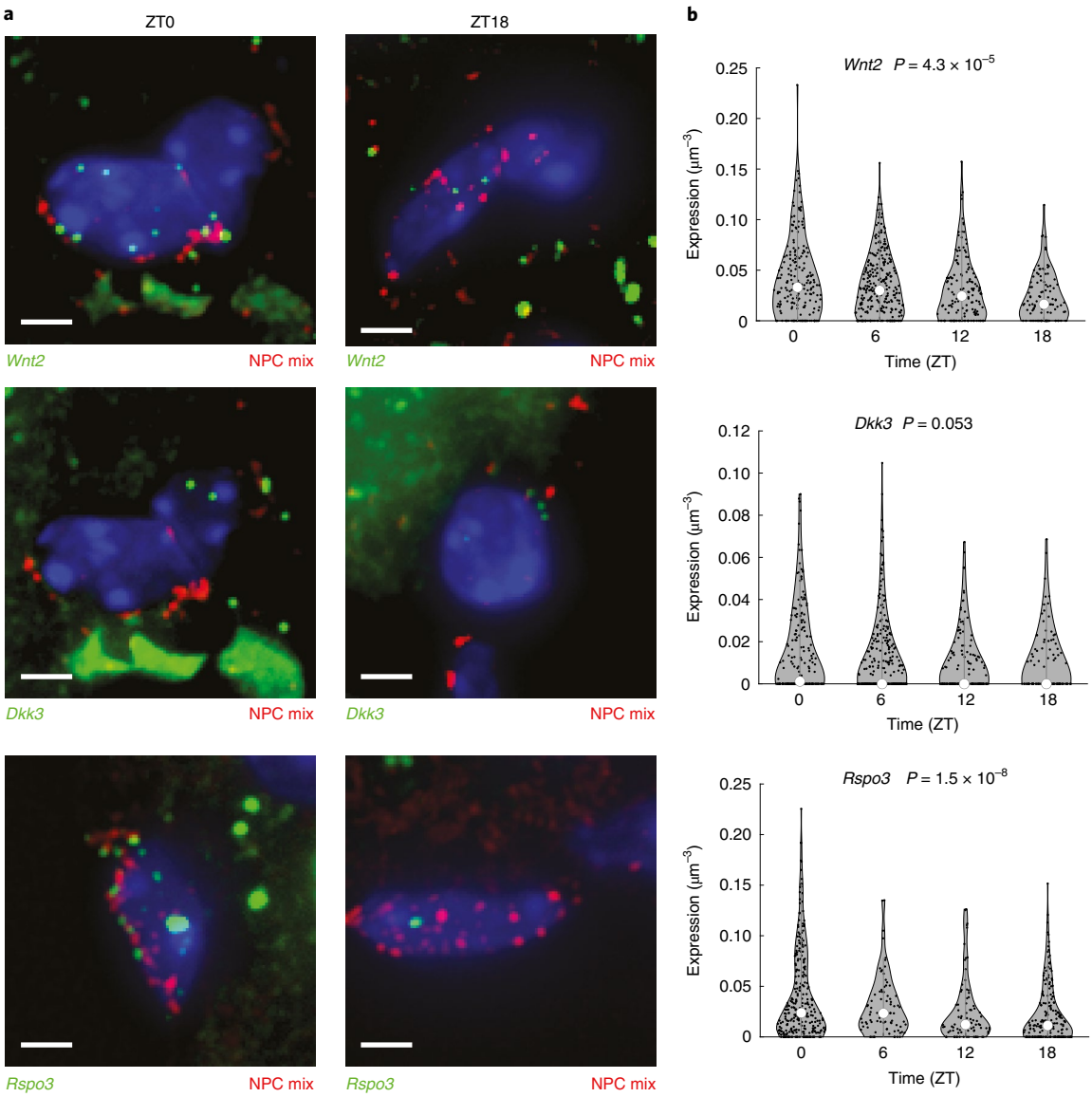

Fig. 7 | Wnt targets could be explained by rhythmically expressed Wnt ligands from NPCs. a, Representative smFISH images of *Wnt2*, *Dkk3* and *Rspo3* expression at ZT0 (left) and ZT18 (right), shown in green. Markers of NPCs are shown in red (Methods). Nuclei are stained in blue (DAPI). Scale bars, 2 μm. **b**, Violin plots representing quantitative analysis of smFISH images ($n = 1{,}420$ cells from 189 central veins of at least 2 mice per time point). *Wnt2*, *Dkk3* and *Rspo3* transcripts are quantified in NPCs lining the central vein (Methods). mRNA expression is in smFISH dots per μm^3. *P* values are obtained from Kruskal–Wallis test.

In this study, we chose to focus on the parenchymal cells in the liver, the hepatocytes, for which smFISH data on landmark zonated genes were readily available, which enabled reconstruction of spatio-temporal mRNA profiles from scRNA-seq[8]. Zonation profiles of other cell types in the liver may be obtained as well; in fact, static zonation mRNA expression profiles have been obtained for liver endothelial cells, using a paired-cell approach[19] in which mRNA from pairs of attached mouse cells were sequenced, and gene expression from one cell type was used to infer the pairs' tissue coordinates. In addition, ab initio reconstruction methods such as diffusion pseudo time[48] or novoSpaRc[53], in which a zonation coordinate is inferred by assuming that the major axis of variability for a cell type reflects transcriptome-wide gene expression changes associated with zonation, could be used for spatially sparse cell types with no available zonated marker genes, for example stellate or resident immune Kupffer cells. Moreover, it has recently been found that rhythmic gene expression and metabolism in non-hepatocyte cells can be driven both by clocks in hepatocytes via cell–cell communication as well as feeding cycles[13]. Our computational framework for analysing space-time logic of gene expression could be widely applicable in such future studies.

To study whether the observed space-time expression profiles might be regulated by either liver zonation, 24-h rhythms in liver physiology, or both, we developed a mixed-effect model, combined with model selection. This enabled classification of gene profiles into five categories representing different modes of spatio-temporal regulation, from flat to wave-like. To validate these, we performed smFISH in intact liver tissue, which showed largely compatible profiles, although some quantitative differences were observed. These differences most likely reflect the lower sensitivity of RNA-seq, uncertainties in the spatial analysis of smFISH in tissues, as well as known interanimal variability in the physiologic states of individual livers, notably related to the animal-specific feeding patterns[25].

Together, this temporal analysis confirms that a large proportion of gene expression in hepatocytes is zonated[8] or rhythmic[17], and in addition reveals marked spatio-temporal regulation of mRNA levels in mouse liver (Z+R and Z×R genes, comprising 7% of all detected genes according to our criteria). This means that zonated gene expression patterns can be temporally modulated on a circadian scale, or equivalently, that rhythmic gene expression profiles can exhibit sub-lobular structure. The dominant pattern for dually regulated gene was Z+R, which corresponds to additive effects of space and time in log, or multiplicate effects of gene expression levels, and describes genes expression profiles that are compartmentalized in both space and time. In other words, such patterns are characterized by shapes (in space) that remain invariant with time, but whose magnitudes are rhythmically rescaled in time. Or equivalently, the oscillatory amplitude (fold change) and phases are constant along the lobular coordinate, but the mean expression is patterned along the lobule. Such multiplicative effects could reflect the combined actions of transcriptional regulators for the zone and rhythm on promoters and enhancers of Z+R genes. Indeed, gene expression changes induced by several regulators combine multiplicatively[22]. Note that though the (relative) shape of Z+R patterns is invariant in time, threshold-dependent responses that would lie downstream of such genes would then acquire domain boundaries which can shift in time. Similar phenomena are expected for interacting profiles (phase and amplitude modulated) (Z×R) that we observed for a smaller number of genes.

As has been shown by us and others[27,28], rhythms at the protein level are typically damped and phase-delayed compared with the cognate mRNA rhythms, depending on the protein half-lives. Indeed, longer protein half-lives imply smaller oscillatory amplitudes and longer delays between mRNA and protein accumulation[14]. Analysis of liver proteomes in bulk showed that the number of cyclic proteins is lower than the number of cyclic mRNAs, with delays approaching the predicted maximum of 6 h. Here, we found genes from both Z+R and Z×R that exhibited rhythmic accumulation in bulk proteomics experiments, including genes encoding rate-limiting enzymes, suggesting that patterns dually regulated by space-time have a physiological role in the liver. Moreover, phase delays between the mRNA and protein profiles were as expected. Future studies will utilize emerging spatial proteomics approaches to reconstruct a space-time liver proteomic atlas[54].

In addition to previously discussed zonated liver functions[8], a systematic querying of KEGG pathways highlighted Z+R functions not previously associated with rhythmic liver zonation. The roles and profiles of the corresponding genes allowed us to better understand the spatio-temporal logic of the identified pathways. For instance, we found that the expression levels of both ribosome protein genes (rate-limiting for protein synthesis[32]) and proteasome components (involved in protein degradation) were higher in central hepatocytes. Since the central environment is subject to high concentrations of xenobiotics and hypoxic stress, this could indicate an elevated protein turnover in this region, which would ensure that damaged proteins are rapidly exchanged with new, undamaged proteins. This interpretation is corroborated by the observed increased levels of cytosolic and ER chaperones during the feeding phase, to assist protein synthesis and secretion, thereby counteracting such protein stress.

It has previously been shown that Wnt signalling can explain the zonation of up to a third of the zonated mRNAs[7]. Wnt ligands are secreted by pericentral NPCs, mostly endothelial cells[5,6], forming a graded spatial morphogenetic field. As a result, and as observed in our enrichment analysis, Wnt-activated genes were pericentrally zonated. Moreover, both the scRNA-seq data and previous bulk mRNA and protein measurements showed that Wnt activity is rhythmic in the liver. Our smFISH analysis suggested that temporal fluctuations in the expression of *Wnt2* and *Rspo3*, encoding two key Wnt ligands, secreted by pericentral NPCs might underlie oscillatory and zonated expression of Wnt targets at times near the fasting–feeding transition.

In summary, we demonstrate how liver gene expression can be quantitatively investigated with spatial and temporal resolution and how liver functions are compartmentalized along these two axes. Our approach could be used to reconstruct spatio-temporal gene expression patterns in other zonated tissues such as the intestine and kidney[3].

Methods

Animals and ethics statement. All animal care and handling were approved by the Institutional Animal Care and Use Committee of WIS and by the Canton de Vaud laws for animal protection (authorization VD3197.b). Male (C57BL/6JOlaHsd) mice aged of 6 weeks, housed under reverse-phase cycle and under ad libitum feeding (Teklad Global 18% Protein Rodent Diet) were used to generate scRNA-seq data of hepatocytes and for smFISH. Littermate controls were used for the ZT6 and ZT18 time points. Male mice between 8 and 10 weeks old (C57BL/6J), housed under a 12:12 light–dark cycle, and that had access to food only during the night (Kliba Nafag 3242 Breeding, Vitamin-fortified, irradiated >25 kGy) were used for smFISH of circadian clock genes (Reporting Summary).

Hepatocytes isolation and single-cell RNA-seq. Liver cells were isolated using a modified version of the two-step collagenase perfusion method of Seglen[55]. The tissue was digested with Liberase Blendzyme 3 recombinant collagenase (Roche Diagnostics), according to the manufacturer's instructions. To enrich for hepatocytes, we applied a centrifuge step at 30*g* for 3 min to pull down all hepatocytes while discarding most of the NPCs that remained in the supernatant. We next enriched for live hepatocytes by 2 cycles of Percoll gradient; the hepatocytes pellet was resuspended in 25 ml of PBS, and Percoll was added for a final concentration of 45% and mixed with the hepatocytes. Dead cells were discarded after a centrifuge step (70*g* for 10 min) and cells were resuspended in 10 cells buffer (1× PBS, 0.04% BSA), and then directly went into the 10x pipeline. The cDNA library was prepared with the V2 chemistry of 10x Genomics Chromium system according to manufacturer's instructions, and sequencing was done with Illumina Nextseq 500 at estimated depth of 40,000 reads per cell. Overall, independent libraries were prepared at ZT0 ($n=3$ biological replicates from individual mice), ZT6 ($n=2$), ZT12 ($n=3$) and ZT18 ($n=2$).

Conceivably, the dissociation of liver tissue into individual cells and the purification of hepatocytes are relatively lengthy processes and may thus lead to alterations in mRNA expression. While it has been shown that mRNA levels do not change much during the purification and 24-h cultivation of hepatocytes[56], transcription rates on the other hand can be diminished by 8- to nearly 100-fold during this process[57]. This difference between nascent transcript and mature mRNA levels can be explained by the relatively long half-lives of liver-specific RNAs. In our case, the time needed from the dissociation of the tissue until the cell lysis was approximately 1 h, and the cells were not placed in culture. Since we were measuring mature transcripts, with half-lives in the range of typically 1–5 h (Extended Data Fig. 2f), the changes in mRNA levels due to the protocol remained contained. In particular, the scRNA-seq of cells carried the typical hepatocyte gene expression signatures, for example genes such as *Alb* or *Apoa2* rank at the second and fifth position genome-wide. As further validation, we compared our reconstructed gene expression zonation profiles with the zonation profiles from the massively validated zonation study of ref. [8], which revealed a near-perfect agreement (Extended Data Fig. 1f).

Filtering of raw scRNA-seq data. The initial data analysis was done in R v3.4.2 using Seurat v2.1.0 (ref. [58]). Each expression matrix was filtered separately to remove dead, dying and low-quality cells. We first kept only genes that were expressed in at least five cells in any of the ten samples. We then defined a set of valid cells with more than 500 expressed genes and between 1,000 and 10,000 unique molecular identifiers (UMIs), and second an additional expression matrix with cells having between 100 and 300 UMIs, which was used for background estimation (Extended Data Fig. 1a). Other UMI filters have been tried, but yielded equally or less-reliable profiles. The mean expression of each gene was then calculated for the background dataset and subtracted from the set of valid cells. This was subsequently filtered to include only hepatocytes by removing cells with expression of non-parenchymal liver cell genes. Next, the cells were filtered on the basis of the fraction of mitochondrial gene expression. First, expression levels in each cell were normalized by the sum of all genes excluding mitochondrial and major urinary protein (*Mup*) genes. Indeed, as mitochondria are more abundant in periportal hepatocytes, the expression of mitochondrial genes is higher in this area[59]; since these genes are very highly expressed, including them would reduce the relative expression of all other genes based on the cell's lobular location. *Mup* genes are also highly abundant, and mapping their reads to a reference sequence

is unreliable due to their high sequence homology[60]. Moreover, *Mup* genes encode pheromones that vary greatly between individuals to facilitate individual recognition[61].

Mitochondrial content is often used to remove non-viable cells[62]. The mitochondrial content of sequenced hepatocytes exhibited a bimodal behaviour (Extended Data Fig. 1b). To identify the range of mitochondrial fractions that included viable hepatocytes, we used an intrinsic property of hepatocytes, which is the anticorrelation of the pericentral landmark gene *Cyp2e1* and the periportal landmark gene *Cyp2f2* (ref. [7]) (Extended Data Fig. 1c). We found that hepatocytes with mitochondrial fraction in the range of 9–35% exhibited an almost perfect anticorrelation between *Cyp2e1* and *Cyp2f2* (Extended Data Fig. 1d,e), suggesting that these are the best quality, and we consequently kept hepatocytes within this range of mitochondrial content for further analysis.

***t*-SNE clustering.** To validate that the expected spatial and temporal axes of variation are present in the scRNA-seq data, we generated a low-dimensional representation of all cells using the standard *t*-SNE[63], a non-linear dimensionality-reduction technique that embeds high-dimensional data on a two-dimensional plane such that points that are similar in high-dimensional space are close together on the two-dimensional representation. We then coloured cells either by their position along the central-portal axis, or by time of day.

Spatial reconstruction of zonation profiles from scRNA-seq data. *Choice of landmark genes.* The reconstruction algorithm relies on a priori knowledge about the zonation of a small set of landmark genes to infer the location of the cells. Reference [8] used smFISH to determine the zonation pattern in situ of six such landmark genes and used them to reconstruct the spatial profiles of all other genes at a single time point. Since we here aimed at reconstructing zonation profiles at different time points, we could not rely on those landmark genes, which might be subject to temporal regulation. Therefore, we used an alternative strategy where we selected landmark zonated genes from ref. [8] ($q<0.2$), with the additional constraints that those should be highly expressed (mean expression in fraction UMI of more than 0.01% and less than 0.1%), and importantly vary little across mice and time. Specifically, we calculated the variability in the mean expression (across all layers) among all mice for every gene and removed genes with ≥10% variability. This yielded 27 central (*Akr1c6*, *Alad*, *Blvrb*, *C6*, *Car3*, *Ccdc107*, *Cml2*, *Cyp2c68*, *Cyp2d9*, *Cyp3a11*, *Entpd5*, *Fmo1*, *Gsta3*, *Gstm1*, *Gstm6*, *Gstt1*, *Hpd*, *Hsd17b10*, *Inmt*, *Iqgap2*, *Mgst1*, *Nrn1*, *Pex11a*, *Pon1*, *Psmd4*, *Slc22a1*, *Tex264*) and 28 portal (*Afm*, *Aldh1l1*, *Asl*, *Ass1*, *Atp5a1*, *Atp5g1*, *C8a*, *C8b*, *Ces3b*, *Cyp2f2*, *Elovl2*, *Fads1*, *Fbp1*, *Ftcd*, *Gm2a*, *Hpx*, *Hsd17b13*, *Ifitm3*, *Igf1*, *Igfals*, *Khk*, *Mug2*, *Pygl*, *Sepp1*, *Serpina1c*, *Serpina1e*, *Serpind1*, *Vtn*) landmark genes.

Reconstruction algorithm. The reconstruction algorithm is based on the algorithm in ref. [8] and was used in the modified version from ref. [19]. Briefly, the expression of each landmark gene was normalized to its maximal expression over all cells. Then, for each cell, we divided the summed expression of all portal landmark genes by the summed expression of all portal and central landmark genes, resulting in a value μ_i between 0 and 1, which we used as the cell location in the liver lobule. We then compared the obtained μ_i with the distributions of cell locations from each of the layers from ref. [8], which yielded a matrix in which every cell has a given probability to belong to a given layer. These weights were then used to compute the mean expression of all genes in a particular layer. The procedure was applied independently on each mouse, yielding ten spatial gene expression profiles for each gene, given as fraction of UMI per cell.

Spatio-temporal analysis of liver gene expression profiles. *Data.* Each profile for the 14,678 genes includes 8 layers from the pericentral to the periportal zone and 4 time points: ZT0 ($n=3$ biological replicates from individual mice), ZT6 ($n=2$), ZT12 ($n=3$) and ZT18 ($n=2$). The expression levels (noted as x) are then log-transformed as follows:

$$y = \log_2(x+\Delta) - B \tag{1}$$

The offset $\Delta = 1\times10^{-4}$ buffers variability in genes with low expression, while the shift $B=-\log_2(11\times10^{-5})$ changes the scale so that $y=0$ corresponds to about 10 mRNA copies per cell (we expect on the order of 1 M mRNA transcripts per liver cell).

Reference genes. For ease of interpretation (Fig. 2 and Extended Data Fig. 2), we used a set of reference circadian genes and a set of reference zonated genes, highlighted in several figures.

The reference core circadian clock and clock output genes are the following: *Bmal1*, *Clock*, *Npas2*, *Nr1d1*, *Nr1d2*, *Per1*, *Per2*, *Cry1*, *Cry2*, *Dbp*, *Tef*, *Hlf*, *Elovl3*, *Rora* and *Rorc*.

The reference zonated genes are the following: *Glul, Ass1*, *Asl*, *Cyp2f2*, *Cyp1a2*, *Pck1*, *Cyp2e1*, *Cdh2*, *Cdh1*, *Cyp7a1*, *Acly*, *Alb*, *Oat*, *Aldob* and *Cps1*.

Gene expression variance in space and time. To analyse variability in space and time (Fig. 2a) we computed, for each gene, the spatial variance V_x and the temporal variance V_T. Let $y_{x,t,j}$ represent the expression profile, with j the replicate index, $t\in\{1,2,\ldots,N_t\}$ the time index, and $x\in\{1,2,\ldots,N_x\}$ the layer index. Then, V_x and V_T are computed as follows:

$$V_X = \frac{1}{N_t}\sum_t \frac{\sum_x\left[\sum_j\left(y_{x,t,j}-\frac{1}{N_x}\sum_x y_{x,t,j}\right)\right]^2}{N_j^2 N_x} \tag{2}$$

$$V_T = \frac{1}{N_x}\sum_x \frac{\sum_t\left[\sum_j\left(y_{x,t,j}-\frac{1}{N_t}\sum_t y_{x,t,j}\right)\right]^2}{N_j^2 N_t} \tag{3}$$

Thus, the spatial variance V_x is computed along the space (and averaged over the replicates) for each time condition, and then averaged over time. The procedure is similar, symmetrically, for V_t.

Gene filtering. For the analyses in Fig. 2, we selected transcripts that were reproducible between replicates and were sufficiently highly expressed (see scatterplot in Extended Data Fig. 2d). To assess reproducibility across replicates, we computed the average relative variance of the spatio-temporal profiles over the replicates:

$$V_J = \frac{\frac{1}{N_xN_t}\sum_{x,t}\left[\frac{1}{N_j}\sum_j\left(y_{x,t,j}-\frac{1}{N_j}\sum_j y_{x,t,j}\right)^2\right]}{\frac{1}{N_xN_tN_j}\sum_{x,t,j}\left[\left(y_{x,t,j}-\frac{1}{N_xN_tN_j}\sum_{x,t,j} y_{x,t,j}\right)^2\right]} \tag{4}$$

We considered genes with values below 50% (Extended Data Fig. 2). To filter genes with low expression, we required the maximum expression level across layers and time points to exceed 1×10^{-5} (fraction of UMIs) which corresponds to $y=0$ or about 10 copies of mRNA per cell. While this was quite more permissive than previous scRNA-seq studies, it allowed us to keep most reference circadian and zonated genes. However, scRNA-seq has limited sensitivity, and some potentially important genes may have been removed in the filtering process. In the end, our filters kept 5,085 genes (1,437 were removed due to low expression, 4,733 due to high variance and 3,543 due to both), which were then used for subsequent analyses.

Mixed-effect model for spatio-temporal mRNA profiles. Since the data are longitudinal in space (eight layers measured in each animal), modelling the space-time profiles required the use of mixed-effect models. To systematically analyse the spatio-temporal mRNA profiles, we used a parameterized function. Specifically, the model uses sine and cosine functions for the time, and polynomials (up to degree 2) for space. Possible interaction between space and time are described as space-dependent oscillatory functions, or equivalently, time-dependent polynomial parameters. Our model for the transformed mRNA expression y reads:

$$y_{x,t,i} = \mu_i + \mu(x) + a(x)\cos(\omega t) + b(x)\sin(\omega t) + \varepsilon_{x,t,\mathrm{i}} \tag{5}$$

Here t is the time, x the spatial position along the liver layers and $i\in\{1,2,\ldots,10\}$ the animal index. This function naturally generalizes harmonic regression, often used for analysis of circadian gene expression[25], by introducing space-dependent coefficients:

$$\begin{cases}\mu(x) = \mu_0 + \mu_1P_1(x) + \mu_2P_2(x)\\ a(x) = a_0 + a_1P_1(x) + a_2P_2(x)\\ b(x) = b_0 + b_1P_1(x) + b_2P_2(x)\end{cases}$$

Here, P_1 and P_2 are the Legendre polynomials of degrees 1 and 2, respectively; μ_0, μ_1 and μ_2 represent the static zonation profile, a_0 and b_0 represent the global (space-independent) rhythmicity of the gene and a_1, a_2, b_1 and b_2 represent layer-dependent rhythmicity. $\varepsilon_{x,t,j}$ is a Gaussian noise term with its s.d. being σ. In addition to the fixed-effect parameters described so far, we introduced a mouse-specific random-effect μ_i (with zero mean). This parameter groups the dependent layer measurements (obtained in the same animal) and thereby properly adjusts the biological sample size for the rhythmicity analysis.

Phases φ (related to peak times t through $t=\varphi\times24/2\pi$) and amplitudes A for each profile can then be computed for any layer from the coefficients $a(x)$ and $b(x)$:

$$\varphi(x) = \arctan2(b(x),a(x)) \quad A(x) = \sqrt{a(x)^2+b(x)^2} \tag{6}$$

Note that peak-to-trough difference is $2A(x)$. The peak-to-trough ratio or fold change of the original expression levels is then $2^{2A(x)}$. We also note that an equivalent writing of the model formulates the problem in terms of time-dependent zonation parameters instead of space-dependent rhythmicity:

$$y_{x,t,i} = \mu_i + \mu_0(t) + \mu_1(t)P_1(x) + \mu_2(t)P_2(x) + \varepsilon_{x,t,i} \tag{7}$$

where:

$$\begin{cases} \mu_0(t) = \mu_0 + a_0\cos(\omega t) + b_0\sin(\omega t) \\ \mu_1(t) = \mu_1 + a_1\cos(\omega t) + b_1\sin(\omega t) \\ \mu_2(t) = \mu_2 + a_2\cos(\omega t) + b_2\sin(\omega t) \end{cases}$$

In this study, we fixed $\omega = \frac{2\pi}{24h}$ because the animals were entrained in a 24-h light–dark cycle and the low time resolution would prevent us from studying ultradian rhythms.

The model parameters, including the variance of the random effects and Gaussian noise strength σ, are estimated for each gene using the fit function from the Python library StatsModels (version 0.9.0). Nelder-Mead was chosen as the optimization method, and the use of a standard likelihood was favoured over the REML likelihood to allow for model comparison[64]. To prevent overfitting of the gene profiles, we added a noise offset $\sigma_0 = 0.15$ ($\log_2$) to the estimated noise σ, in the expression of the likelihood function used in the mixed-effect model optimization.

Depending on the gene, the model presented in equations (5) and (7) may be simplified by setting all or some of the (fixed) parameters to 0. For example, a non-oscillatory gene profile would normally have non-significant a_j and b_j parameters. In practice, considering the fixed effects, 2^9 sub-models of various complexity can be generated. However, we added a few reasonable requirements to reduce the number of models. First, the intercept μ_0 must be present in every model. Similarly, the parameters a_0 and b_0, providing a global rhythm, must be present in every rhythmic model. Finally, the parameters a_j and b_j for $j = 0,1,2$ must be paired to ensure a proper phase definition (equation (6)).

The models can then be classified in different categories, depending on the retained (non-zero) parameters (Fig. 2c):

- The model comprising only the intercepts μ_0 and μ_i, termed flat or noisy (F/N).
- The models comprising only the intercepts and zonation parameters: μ_1 and/or μ_2, termed purely zonated (Z).
- The models comprising only the intercepts and rhythmic parameters: a_0 and b_0, termed purely rhythmic (R).
- The models comprising only the intercepts, zonated parameters and rhythmic parameters: μ_1 and/or μ_2, and a_0,b_0, termed independent (Z + R).
- The models comprising interaction parameters: a_j and b_j for $j = 1,2$, termed interacting (Z × R).

Note that we only plot the fixed effects in the predicted gene profiles. The Bayesian Information Criterion (BIC) is then used for model selection, enabling selection of the most parsimonious model for each gene. Consequently, the F/N class also contains noisy profiles, since genes that are not well fitted with any complex model will then be assigned to the simplest model. Additionally, it appears that, for some profiles, several competing models can result in close BIC values (see for example the discussion on *Clock* and *Cry*1 in the Results). Therefore, when assigning hard classes, if some models have a relative difference of less than 1% in their BIC, we systematically keep the most complex model. Moreover, we also assigned probabilities to the different categories (F, Z, R, Z + R and Z × R), computed as Schwartz BIC weights[65], which is useful in case of ambiguous classification (Supplementary Table 2). All best fits with their parameter values are listed in Supplementary Table 1.

Bulk RNA-seq dataset. A bulk liver RNA-seq dataset was obtained from ref. [25]. These data was obtained from a sampling every 2 h for 24 h, with 4 replicates per time condition. For Extended Data Fig. 2e, we only compared genes for which rhythmicity did not change across layers, namely the R and Z + R categories. Note that since the scRNA-seq data has a lower temporal resolution and fewer replicates per time point, we found overall less rhythmic genes.

To assess gene rhythmicity, we used harmonic regression on the log-transformed profiles. Using the same notation as above, we define the two following models:

$$\{y_{t,i} = \mu + \varepsilon \quad (9)$$

$$\{y_{t,i} = \mu + a\cos(\omega t) + b\sin(\omega t) + \varepsilon \quad (10)$$

We then fit equation (8) and equation (9) to every transcript. Depending on the figure, we either kept the model with the lowest BIC (Extended Data Fig. 2e, for which we also compute the circular correlation coefficient[66]) or the ones having a significant rhythmicity according to a F test (Fig. 6).

KEGG pathway enrichment analysis. Functional annotation clustering from Enrichr[67] for the categories F/N, Z and Z + R (which is then subdivided in central and portal), Zc + R (central zonated and rhythmic), Zp + R (portal zonated and rhythmic) and finally R was ran (https://maayanlab.cloud/Enrichr/) with standard parameters, using the standard KEGG 2019 Mouse set of pathways. The enriched pathways (adjusted P value < 0.1, standard Enrichr output test) were then further annotated to compute, for example the number of central/portal genes in each category and the phase of each gene. This analysis is available Supplementary Table 3.

smFISH. Analysis of Z + R and Z × R genes (Stellaris smFISH probes). Preparation of probe libraries, the hybridization procedure and imaging conditions were previously described[19]. Briefly, smFISH probe libraries were coupled to TMR, Alexa594 or Cy5. Cell membranes were stained with Alexa Fluor 488 –conjugated phalloidin (Rhenium A12379) that was added to GLOX buffer[68]. The portal node was identified morphologically on DAPI images based on bile ductile, and the central vein was identified using smFISH for Glul in TMR, included in all hybridizations. Images were taken as scans spanning the portal node to the central vein. Images were analysed using ImageM[68]. Quantifications of zonation profiles at different circadian time points were generated by counting dots and dividing the number of dots in radial layers spanning the portal–central axis by the layer volume.

Temporal analysis of circadian genes (RNA scope smFISH probes). smFISH of R genes were done on fresh-frozen liver cryosections (8 µm) embedded in O.C.T. Compound (Tissue-Tek; Sakura-Finetek), sampled every 3 h (from ZT0 to ZT21). RNAscope probes for *Bma1l* mRNA (Mm-Arntl, catalogue no. 438748-C3) and *Per1* mRNA (Mm-Per1, catalogue no. 438751) were used, according to the manufacturer's instructions for the RNAscope Fluorescent Multiplex V1 Assay (Advanced Cell Diagnostics). To detect the central vein, an immunofluorescence of glutamine synthetase (ab49873, Abcam, diluted 1:2,000 in PBS/BSA 0.5%/Triton X-100 0.01%) was done together with smFISH. Nuclei were counterstained with DAPI, and sections were mounted with ProLong Gold Antifade Mountant. Liver sections were imaged with a Leica DM5500 widefield microscope and an oil-immersion ×63 objective. *Z*-stacks were acquired (0.2 µm between each *Z* position), and mRNA transcripts were quantified using ImageJ, as described previously in ref. [50]. Pericentral (PC) and periportal (PP) veins were manually detected on the basis of glutamine synthetase immunofluorescence or on bile ducts (DAPI staining). The Euclidean distance between two veins and the distance from the vein of each mRNA transcript were calculated. mRNA transcripts were assigned to a PP or PC zone if the distance from the corresponding vein was smaller than one-third of the distance between the PP and PC veins (ranging from 50 to 130 µm).

Wnt2, Rspo3 and Dkk3 expression in non-parenchymal cells (Stellaris smFISH probes). Preparation of probe libraries, hybridization protocol and imaging conditions were previously described[19]. The *Aqp1*, *Igfbp7 and Ptprb* probe libraries were coupled to TMR, the *Wnt2* library was coupled to *Alexa594* and the *Dkk3* or *Rspo3* library were coupled to *Cy5*. Cell membranes were stained with Alexa Fluor 488 coupled to phalloidin (Rhenium A12379) that was added to GLOX buffer[68]. The central vein was identified on the basis of morphological features inspected in the DAPI and phalloidin channels and the presence of Wnt2-mRNA (detected by smFISH). Central vein niche NPCs were identified by co-staining of *Aqp1*, *Igfbp7* and *Ptprb*. The central vein area was imaged and the images were analysed using ImageM[68]. We counted dots of *Wnt2*, *Rspo3* and *Dkk3* expression (corresponding to single mRNA molecules) in NPCs lining the central vein and removed background dots larger than 25 pixels. We then divided the dot count by the segmented cell volume. In total, 1,420 NPCs from 189 central veins of at least 2 mice per time point (ZT0, ZT6, ZT12, ZT18) were imaged, and a Kruskal–Wallis test based on the mean mRNA dot concentration in each cell was performed to compare the ZT0 and ZT18 time points.

Reporting Summary. Further information on research design is available in the Nature Research Reporting Summary linked to this article.

Data availability

All scRNA-seq data has been deposited in GEO with accession code GSE145197. Reconstructed spatio-temporal gene profiles are available as Matlab files at https://github.com/naef-lab/Circadian-zonation The whole dataset of gene profiles along with the analysis is available online as a web-application at the URL https://czviz.epfl.ch/. The application was built in Python using the library Dash by Plotly (version 1.0).

Code availability

The code for fitting the mixed-effects models and generating the main figures is available at https://github.com/naef-lab/Circadian-zonation
Details regarding the statistics, software and data are provided in the Reporting Summary.

Received: 5 March 2020; Accepted: 12 November 2020;
Published online: 11 January 2021

References

1. Gebhardt, R. Metabolic zonation of the liver: Regulation and implications for liver function. *Pharmacol. Ther.* **53**, 275–354 (1992).
2. Hoehme, S. et al. Prediction and validation of cell alignment along microvessels as order principle to restore tissue architecture in liver regeneration. *Proc. Natl Acad. Sci. USA* **107**, 10371–10376 (2010).

3. Ben-Moshe, S. & Itzkovitz, S. Spatial heterogeneity in the mammalian liver. *Nat. Rev. Gastroenterol. Hepatol.* **16**, 395–410 (2019).
4. Colnot, S. & Perret, C. in *Molecular Pathology of Liver Diseases* Vol. 5 (ed. Monga, S. P. S.) 7–16 (Springer, 2011).
5. Wang, B., Zhao, L., Fish, M., Logan, C. Y. & Nusse, R. Self-renewing diploid Axin2^{+} cells fuel homeostatic renewal of the liver. *Nature* **524**, 180–185 (2015).
6. Planas-Paz, L. et al. The RSPO–LGR4/5–ZNRF3/RNF43 module controls liver zonation and size. *Nat. Cell Biol.* **18**, 467–479 (2016).
7. Jungermann, K. & Kietzmann, T. Zonation of parenchymal and nonparenchymal metabolism in liver. *Annu. Rev. Nutr.* **16**, 179–203 (1996).
8. Halpern, K. B. et al. Single-cell spatial reconstruction reveals global division of labour in the mammalian liver. *Nature* **542**, 352–356 (2017).
9. Dibner, C., Schibler, U. & Albrecht, U. The mammalian circadian timing system: organization and coordination of central and peripheral clocks. *Annu. Rev. Physiol.* **72**, 517–549 (2010).
10. Green, C. B., Takahashi, J. S. & Bass, J. The meter of metabolism. *Cell* **134**, 728–742 (2008).
11. Yeung, J. & Naef, F. Rhythms of the genome: circadian dynamics from chromatin topology, tissue-specific gene expression, to behavior. *Trends Genet.* **34**, 915–926 (2018).
12. Maury, E., Ramsey, K. M. & Bass, J. Circadian rhythms and metabolic syndrome: from experimental genetics to human disease. *Circ. Res.* **106**, 447–462 (2010).
13. Guan, D. et al. The hepatocyte clock and feeding control chronophysiology of multiple liver cell types. *Science* **369**, 1388–1394 (2020).
14. Mermet, J., Yeung, J. & Naef, F. Systems chronobiology: global analysis of gene regulation in a 24-hour periodic world. *Cold Spring Harb. Perspect. Biol.* **9**, a028720 (2017).
15. Zhang, R., Lahens, N. F., Ballance, H. I., Hughes, M. E. & Hogenesch, J. B. A circadian gene expression atlas in mammals: implications for biology and medicine. *Proc. Natl Acad. Sci. USA* **111**, 16219–16224 (2014).
16. Sobel, J. A. et al. Transcriptional regulatory logic of the diurnal cycle in the mouse liver. *PLoS Biol.* **15**, e2001069 (2017).
17. Vollmers, C. et al. Time of feeding and the intrinsic circadian clock drive rhythms in hepatic gene expression. *Proc. Natl Acad. Sci. USA* **106**, 21453–21458 (2009).
18. Yeung, J. et al. Transcription factor activity rhythms and tissue-specific chromatin interactions explain circadian gene expression across organs. *Genome Res.* **28**, 182–191 (2018).
19. Halpern, K. B. et al. Paired-cell sequencing enables spatial gene expression mapping of liver endothelial cells. *Nat. Biotechnol.* **36**, 962–970 (2018).
20. Bunger, M. K. et al. Mop3 is an essential component of the master circadian pacemaker in mammals. *Cell* **103**, 1009–1017 (2000).
21. Ripperger, J. A., Shearman, L. P., Reppert, S. M. & Schibler, U. CLOCK, an essential pacemaker component, controls expression of the circadian transcription factor DBP. *Genes Dev.* **14**, 679–689 (2000).
22. Beal, J. Biochemical complexity drives log-normal variation in genetic expression. *Eng. Biol.* **1**, 55–60 (2017).
23. McLean, R. A., Sanders, W. L. & Stroup, W. W. A unified approach to mixed linear models. *Am. Stat.* **45**, 54 (1991).
24. Wagenmakers, E.-J. & Farrell, S. AIC model selection using Akaike weights. *Psychon. Bull. Rev.* **11**, 192–196 (2004).
25. Atger, F. et al. Circadian and feeding rhythms differentially affect rhythmic mRNA transcription and translation in mouse liver. *Proc. Natl Acad. Sci. USA* **112**, E6579–E6588 (2015).
26. Kietzmann, T. Metabolic zonation of the liver: the oxygen gradient revisited. *Redox Biol.* **11**, 622–630 (2017).
27. Robles, M. S., Cox, J. & Mann, M. In-vivo quantitative proteomics reveals a key contribution of post-transcriptional mechanisms to the circadian regulation of liver metabolism. *PLoS Genet.* **10**, e1004047 (2014).
28. Mauvoisin, D. et al. Circadian clock-dependent and -independent rhythmic proteomes implement distinct diurnal functions in mouse liver. *Proc. Natl Acad. Sci. USA* **111**, 167–172 (2014).
29. Gebhardt, R. Liver zonation: novel aspects of its regulation and its impact on homeostasis. *World J. Gastroenterol.* **20**, 8491 (2014).
30. Kornmann, B., Schaad, O., Bujard, H., Takahashi, J. S. & Schibler, U. System-driven and oscillator-dependent circadian transcription in mice with a conditionally active liver clock. *PLoS Biol.* **5**, e34 (2007).
31. Reinke, H. et al. Differential display of DNA-binding proteins reveals heat-shock factor 1 as a circadian transcription factor. *Genes Dev.* **22**, 331–345 (2008).
32. Sinturel, F. et al. Diurnal oscillations in liver mass and cell size accompany ribosome assembly cycles. *Cell* **169**, 651–663.e14 (2017).
33. Kietzmann, T., Cornesse, Y., Brechtel, K., Modaressi, S. & Jungermann, K. Perivenous expression of the mRNA of the three hypoxia-inducible factor alpha-subunits, HIF1α, HIF2α and HIF3α, in rat liver. *Biochem. J.* **354**, 531–537 (2001).
34. Ma, D., Panda, S. & Lin, J. D. Temporal orchestration of circadian autophagy rhythm by C/EBPβ: C/EBPβ regulates circadian autophagy rhythm. *EMBO J.* **30**, 4642–4651 (2011).
35. Wang, J. et al. Nuclear proteomics uncovers diurnal regulatory landscapes in mouse liver. *Cell Metab.* **25**, 102–117 (2017).
36. Harper, J. W., Ordureau, A. & Heo, J.-M. Building and decoding ubiquitin chains for mitophagy. *Nat. Rev. Mol. Cell Biol.* **19**, 93–108 (2018).
37. Le Martelot, G. et al. REV–ERBα participates in circadian srebp signaling and bile acid homeostasis. *PLoS Biol.* **7**, e1000181 (2009).
38. Ferrell, J. M. & Chiang, J. Y. L. Short-term circadian disruption impairs bile acid and lipid homeostasis in mice. *Cell. Mol. Gastroenterol. Hepatol.* **1**, 664–677 (2015).
39. Ma, K. et al. Circadian dysregulation disrupts bile acid homeostasis. *PLoS ONE* **4**, e6843 (2009).
40. Yu, L. et al. Disruption of Abcg5 and Abcg8 in mice reveals their crucial role in biliary cholesterol secretion. *Proc. Natl Acad. Sci. USA* **99**, 16237–16242 (2002).
41. Oki, S. et al. ChIP-Atlas: a data-mining suite powered by full integration of public ChIP-seq data. *EMBO Rep.* **19**, e46255 (2018).
42. Gotic, I. et al. Temperature regulates splicing efficiency of the cold-inducible RNA-binding protein gene *Cirbp*. *Genes Dev.* **30**, 2005–2017 (2016).
43. Jakobsson, A., Jörgensen, J. A. & Jacobsson, A. Differential regulation of fatty acid elongation enzymes in brown adipocytes implies a unique role for *Elovl3* during increased fatty acid oxidation. *Am. J. Physiol. Endocrinol. Metab.* **289**, E517–E526 (2005).
44. Burke, Z. D. & Tosh, D. The Wnt/β-catenin pathway: master regulator of liver zonation? *Bioessays* **28**, 1072–1077 (2006).
45. Gougelet, A. et al. T-cell factor 4 and β-catenin chromatin occupancies pattern zonal liver metabolism in mice. *Hepatology* **59**, 2344–2357 (2014).
46. Lavery, D. J. et al. Circadian expression of the steroid 15 α-hydroxylase (*Cyp2a4*) and coumarin 7-hydroxylase (*Cyp2a5*) genes in mouse liver is regulated by the PAR leucine zipper transcription factor DBP. *Mol. Cell. Biol.* **19**, 6488–6499 (1999).
47. Carmon, K. S., Gong, X., Lin, Q., Thomas, A. & Liu, Q. R-spondins function as ligands of the orphan receptors LGR4 and LGR5 to regulate Wnt/beta-catenin signaling. *Proc. Natl Acad. Sci. USA* **108**, 11452–11457 (2011).
48. Aizarani, N. et al. A human liver cell atlas reveals heterogeneity and epithelial progenitors. *Nature* **572**, 199–204 (2019).
49. Brosch, M. et al. Epigenomic map of human liver reveals principles of zonated morphogenic and metabolic control. *Nat. Commun.* **9**, 4150 (2018).
50. Mermet, J. et al. Clock-dependent chromatin topology modulates circadian transcription and behavior. *Genes Dev.* **32**, 347–358 (2018).
51. Le Martelot, G. et al. Genome-Wide RNA polymerase II profiles and RNA accumulation reveal kinetics of transcription and associated epigenetic changes during diurnal cycles. *PLoS Biol.* **10**, e1001442 (2012).
52. Wang, J. et al. Circadian clock-dependent and -independent posttranscriptional regulation underlies temporal mRNA accumulation in mouse liver. *Proc. Natl Acad. Sci. USA* **115**, E1916–E1925 (2018).
53. Nitzan, M., Karaiskos, N., Friedman, N. & Rajewsky, N. Gene expression cartography. *Nature* **576**, 132–137 (2019).
54. Ben-Moshe, S. et al. Spatial sorting enables comprehensive characterization of liver zonation. *Nat. Metab.* **1**, 899–911 (2019).
55. Seglen, P. O. in *Methods in Cell Biology* Vol. 13, Ch. 4 (Elsevier, 1976).
56. Darnell, A. M., Subramaniam, A. R. & O'Shea, E. K. Translational control through differential ribosome pausing during amino acid limitation in mammalian cells. *Mol. Cell* **71**, 229–243.e11 (2018).
57. Clayton, D. F., Harrelson, A. L. & Darnell, J. E. Dependence of liver-specific transcription on tissue organization. *Mol. Cell. Biol.* **5**, 2623–2632 (1985).
58. Satija, R., Farrell, J. A., Gennert, D., Schier, A. F. & Regev, A. Spatial reconstruction of single-cell gene expression data. *Nat. Biotechnol.* **33**, 495–502 (2015).
59. Loud, A. V. A quantitative stereological description of the ultrastructure of normal rat liver parenchymal cells. *J. Cell Biol.* **37**, 27–46 (1968).
60. Kuhn, N. J., Woodworth-Gutai, M., Gross, K. W. & Held, W. A. Subfamilies of the mouse major urinary protein (MUP) multi-gene family: sequence analysis of cDNA clones and differential regulation in the liver. *Nucleic Acids Res.* **12**, 6073–6090 (1984).
61. Hurst, J. L. et al. Individual recognition in mice mediated by major urinary proteins. *Nature* **414**, 631–634 (2001).
62. Ilicic, T. et al. Classification of low quality cells from single-cell RNA-seq data. *Genome Biol.* **17**, 29 (2016).
63. Maaten, Lvander & Hinton, G. Visualizing data using *t*-SNE. *J. Mach. Learn. Res.* **9**, 2579–2605 (2008).
64. Müller, S., Scealy, J. L. & Welsh, A. H. Model selection in linear mixed models. *Stat. Sci.* **28**, 135–167 (2013).
65. Schwarz, G. Estimating the dimension of a model. *Ann. Stat.* **6**, 461–464 (1978).

66. Jammalamadaka, S. R. & SenGupta, A. *Topics in Circular Statistics*. Vol. 5 (World Scientific, 2001).
67. Chen, E. Y. et al. Enrichr: interactive and collaborative HTML5 gene list enrichment analysis tool. *BMC Bioinf.* **14**, 128 (2013).
68. Lyubimova, A. et al. Single-molecule mRNA detection and counting in mammalian tissue. *Nat. Protoc.* **8**, 1743–1758 (2013).

Acknowledgements

We thank D. Mauvoisin for assistance with the animal work, C. Gobet for bioinformatics advice and the EPFL BIOP facility for advice with microscopy. This work was supported by the Rothschild Caesarea Foundation' fund managed by Weizmann Institute and EPFL, a Swiss National Science Foundation Grant 310030_173079 (to F.N.), and the EPFL. S.I. is supported by the Henry Chanoch Krenter Institute for Biomedical Imaging and Genomics, The Leir Charitable Foundations, Richard Jakubskind Laboratory of Systems Biology, Cymerman-Jakubskind Prize, The Lord Sieff of Brimpton Memorial Fund, the Wolfson Foundation SCG, the Wolfson Family Charitable Trust, Edmond de Rothschild Foundations, the I-CORE programme of the Planning and Budgeting Committee and the Israel Science Foundation (grants 1902/12 and 1796/12, the Israel Science Foundation grant no. 1486/16, the Chan Zuckerberg Initiative grant no. CZF2019-002434, the Broad Institute-Israel Science Foundation grant no. 2615/18, the European Research Council (ERC) under the European Union's Horizon 2020 research and innovation programme (grant agreement no. 768956), the Bert L. and N. Kuggie Vallee Foundation and the Howard Hughes Medical Institute (HHMI) international research scholar award.

Author contributions

F.N. and S.I. conceived of the study. K.B.H., J.E.K. and C.H. prepared all the samples and performed the experiments. C.D. and F.N designed the modelling. C.D., J.E.K., K.B.H. and C.H. analyed the data. M.R. and S.M. assisted with the scRNA-seq and smFISH experiments. F.N and S.I. supervised the study. C.D., J.E.K. and F.N. wrote the manuscript. All authors reviewed the manuscript and provided input.

Competing interests

The authors declare no competing interests.

Additional information

Extended data is available for this paper at https://doi.org/10.1038/s42255-020-00323-1.

Supplementary information is available for this paper at https://doi.org/10.1038/s42255-020-00323-1.

Correspondence and requests for materials should be addressed to S.I. or F.N.

Peer review information Primary Handling Editors: George Caputa; Pooja Jha. *Nature Metabolism* thanks Dominic Grun, Ueli Schibler and Jan S. Tchorz for their contribution to the peer review of this work.

Reprints and permissions information is available at www.nature.com/reprints.

Publisher's note Springer Nature remains neutral with regard to jurisdictional claims in published maps and institutional affiliations.

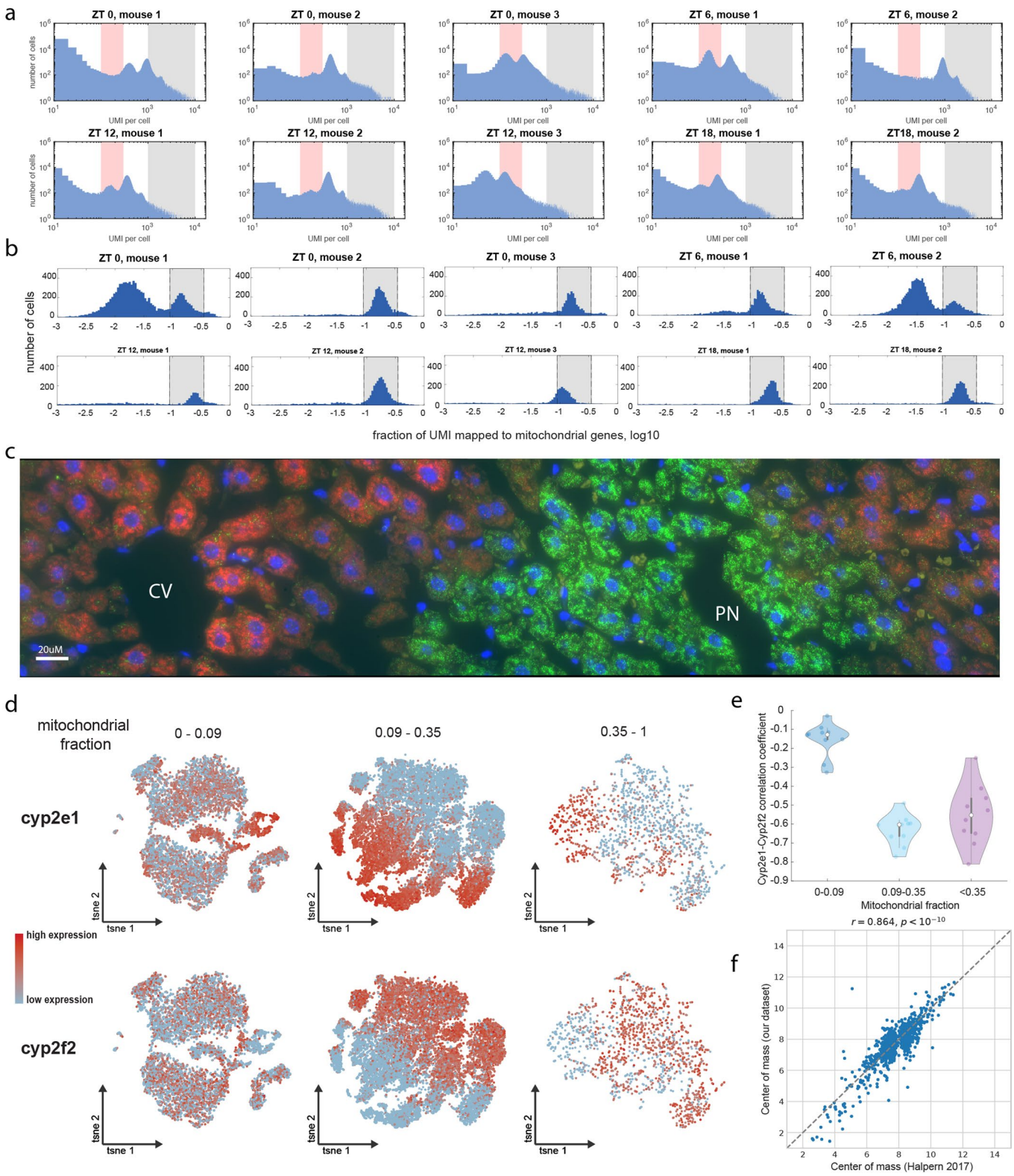

Extended Data Fig. 1 | See next page for caption.

Extended Data Fig. 1 | scRNA-seq pre-processing. a, Histogram of number of UMIs per cell barcode for each mouse. Red patches mark the cells used for background estimation (100-300 UMI/cell barcode), gray patches mark the cells used for downstream analysis (1000-10000 UMI/cell barcode). **b**, Histogram of fraction of all UMIs mapping to mitochondrial genes. Filter used for downstream analysis in grey (0.09–0.35). **c**, smFISH staining of a liver lobule with probes against *Cyp2e1* (red) and *Cyp2f2* (green). CV = central vein, PN = portal node. Overall, the data combine 10 images from from two mice. **d**, Expression of *Cyp2e1* and *Cyp2f2* in cells with different fraction of mitochondrial expression. Three different filters for the fraction of UMIs mapping to mitochondrial genes (0–0.09, 0.09–0.35, 0.35–1) were applied, the data of all mice merged and the resulting datasets visualized as t-SNE plots. **e**, Violin plots for the correlations between *Cyp2e1* and *Cyp2f2* expression in single hepatocyte populations with different filters for fractions of mitochondrial expression. Each dot represents one mouse (n = 10 mice for each distribution) and the shape of the violin represents the density of points. **f**, Comparison of the zonation profiles of Z and Z + R genes obtained in our current study and the previous reconstruction from *Halpern et al.* [8]. Profiles were interpolated to fit 15 layers, where 1 is pericentral and 8 is periportal. Dots indicate the center of mass (expression-weighted lobule layer) of the Z and Z+R genes computed in both datasets, for gene having an average expression of at least 10^{-5} in *Halpern et al.* *r* is the correlation coefficient, *p* the corresponding p-value from a standard linear regression.

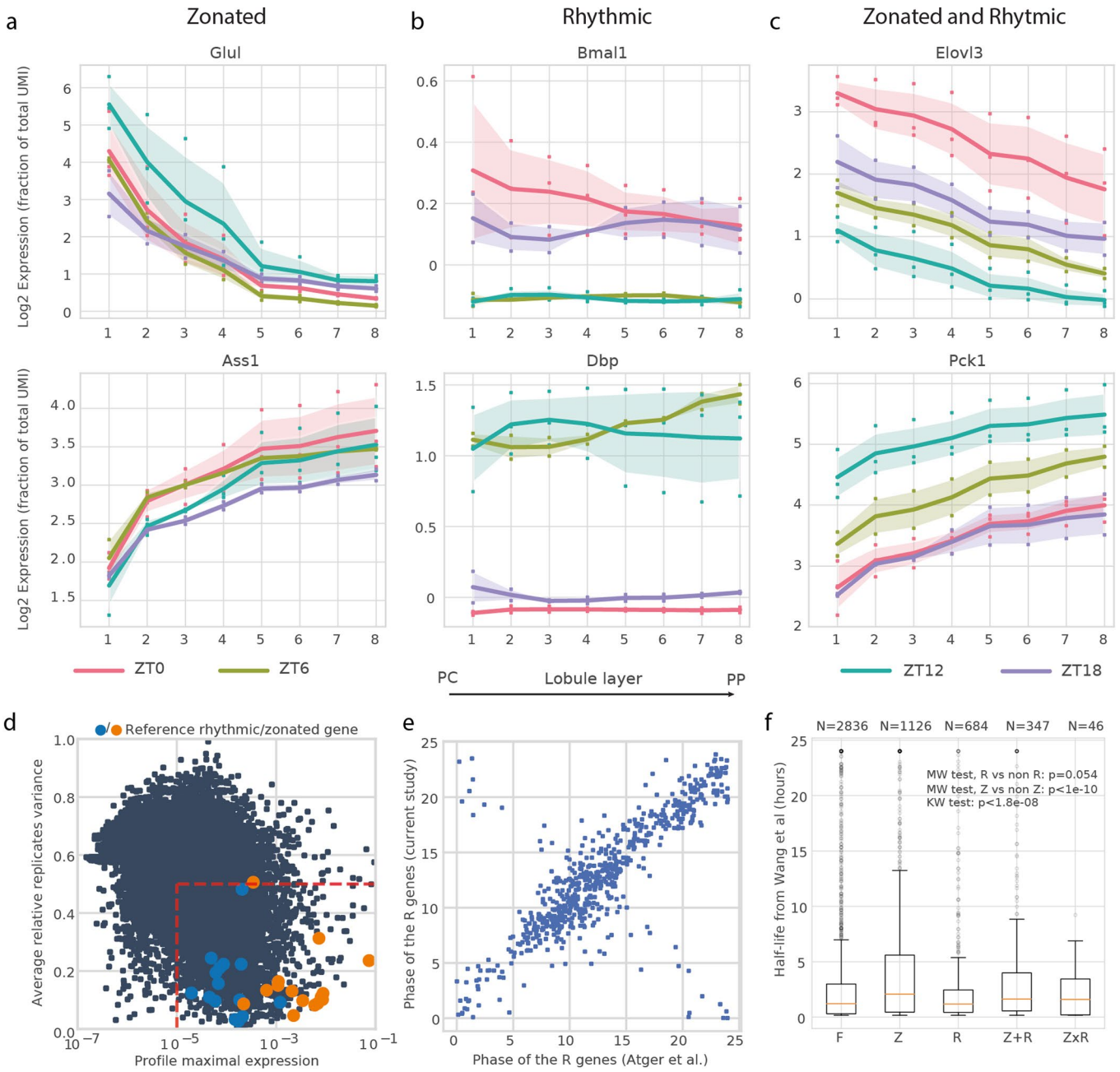

Extended Data Fig. 2 | Log-transformed reconstructed profiles, pre-filtering of the genes and comparison with external datasets. a-c, Expression levels of the reconstructed profiles for the genes from Fig. 1f–h after log-transformation (Methods). Dots in represent data points from the individual mice. Lines represent mean expression per time point. Shaded areas represent one standard deviation (SD) across the mice (n=2 or n=3 depending on the time point, Methods). **d**, Biological variability of gene profiles across independent replicate liver samples, quantified in terms of the average relative replicate variance. 0 shows perfectly reproducible profiles while 1 the most variable genes (Methods). Genes inside the bottom-right box (x-cutoff at 10^{-5}; y-cutoff at 0.5) are selected and contain all but one of the reference genes. Colored dots show reference zonated genes (blue) and reference rhythmic genes (orange). **e**, Comparison of the peak times for rhythmic genes in R and Z+R, with the dataset from *Atger et al. PNAS* [25]. Circular correlation coefficient is 0.746 (Methods). **f**, Boxplot of the mRNA half-lives (data from *Wang, J. et al.* [35]) shows that R genes as a group (median, orange line) are the shortest-lived. Box limits are lower and upper quartiles, whiskers extend up to the first datum greater/lower than the upper/lower quartile plus 1.5 times the interquartile range. Remaining points are marked. MW stands for the two-sided Mann-Whitney test, and KW stands for Kruskal-Wallis test.

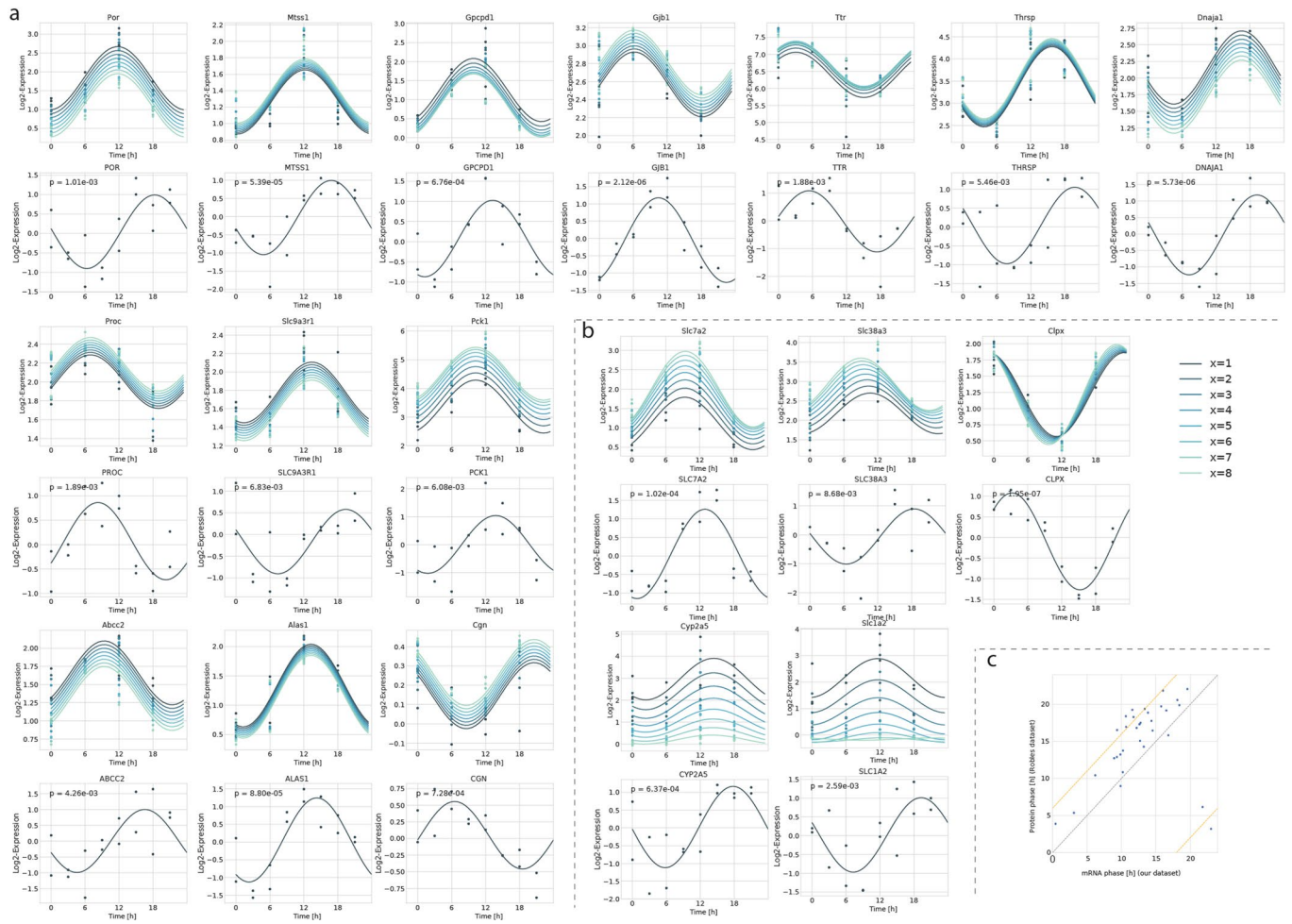

Extended Data Fig. 3 | Z+R and ZxR transcripts with corresponding rhythmic protein accumulation in bulk mass spectrometry data. a-b, Rhythmic proteins corresponding to Z+R (**a**) and ZxR (**b**) transcripts were selected from *Robles et al.*, [27] (from original Supplementary Table 2), and fitted with harmonic regression (p-value of rhythmicity from F-tests are indicated above the plot). Only proteins having a p-value<0.01 are shown. **c**, Scatter plot of the phase of the fits from the transcripts (x-axis) against the phase of the fits from the proteins (y-axis). The diagonal is indicated with a dashed grey line, the theoretical upper bound (6 h) for the delay between mRNA and protein is indicated with a dashed red line. All rhythmic proteins (q<0.2 in the original analysis) are represented.

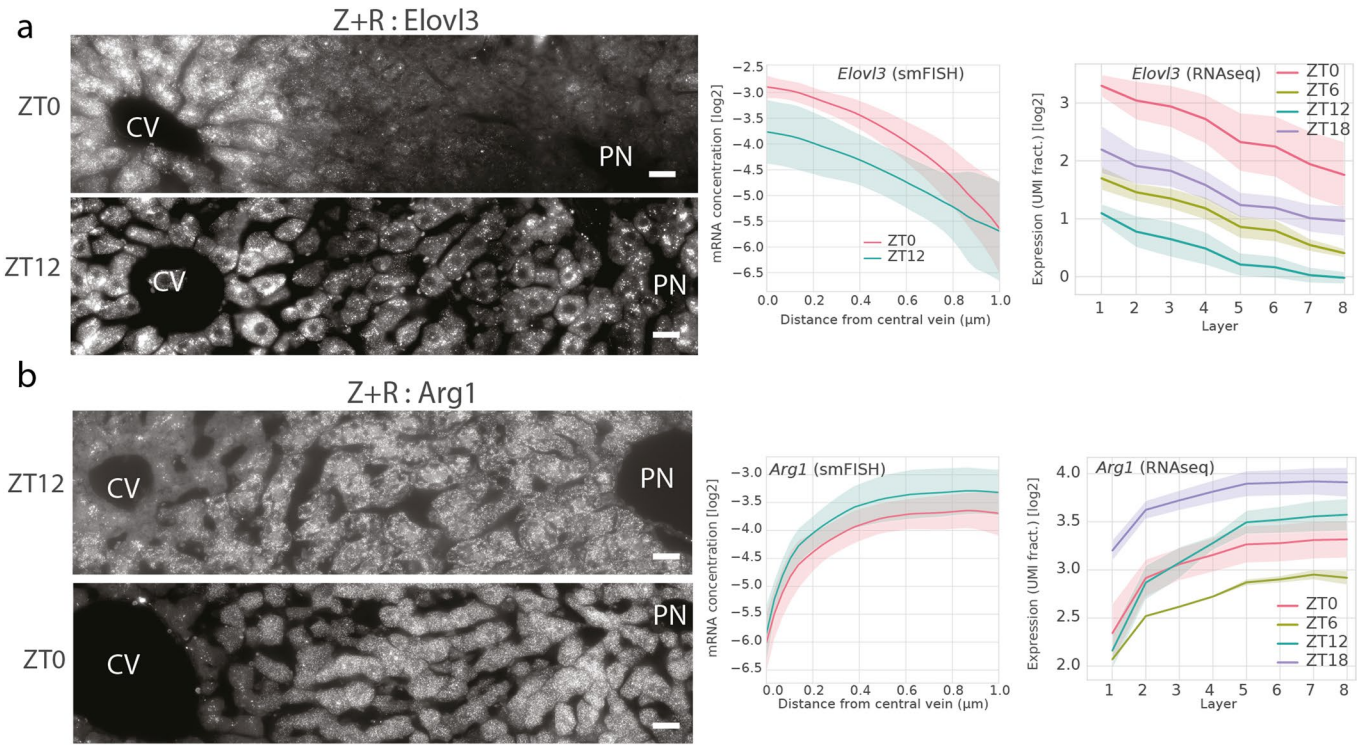

Extended Data Fig. 4 | Additional validations for the Z+R category. a-b, smFISH (Stellaris, Methods) for *Elovl3* (Z+R) and *Arg1* (Z+R). smFISH quantifications were made for ZT0 and ZT12 (Methods). **Left**: representative images at ZT0, ZT12 for *Elovl3* (**a**) or *Arg1* (**b**). Pericentral veins (CV) and a periportal node (PN) are marked. Scale bar - 20 μm. **Right:** quantified profiles for each gene at the two time points from smFISH (top, line plot is the mean number of mRNAs, shaded area indicate SD across twelve images), and scRNA-seq data (bottom, line plot is mean expression, shaded area is SD across mice, n=2 or n=3 depending on the time point, Methods).

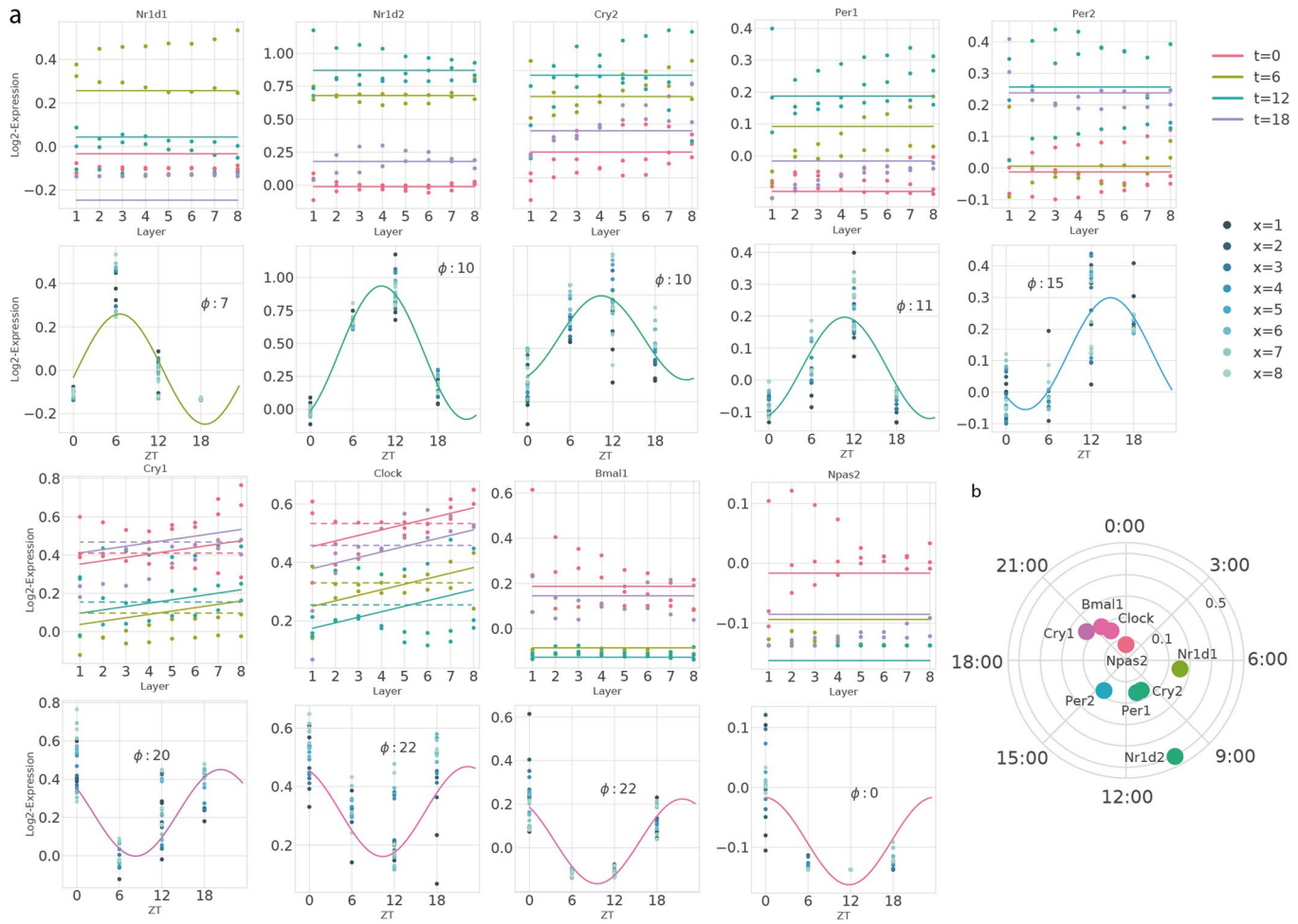

Extended Data Fig. 5 | The core circadian-clock is not zonated. a, Spatial and temporal profiles and fits for circadian core-clock genes. Peak times are indicated on the temporal representation. For the genes *Cry1* and *Clock*, additional dashed lines represent fits for the R model, as the Schwartz BIC weights from the R and Z+R models were close (Supplementary Table 2). **b**, Amplitudes and peak times of the core-clock circadian genes in a polar coordinate representation (clock-wise ZT times are indicated, distance from the center corresponds to the amplitude) show the expected organization of core clock transcript in the liver.

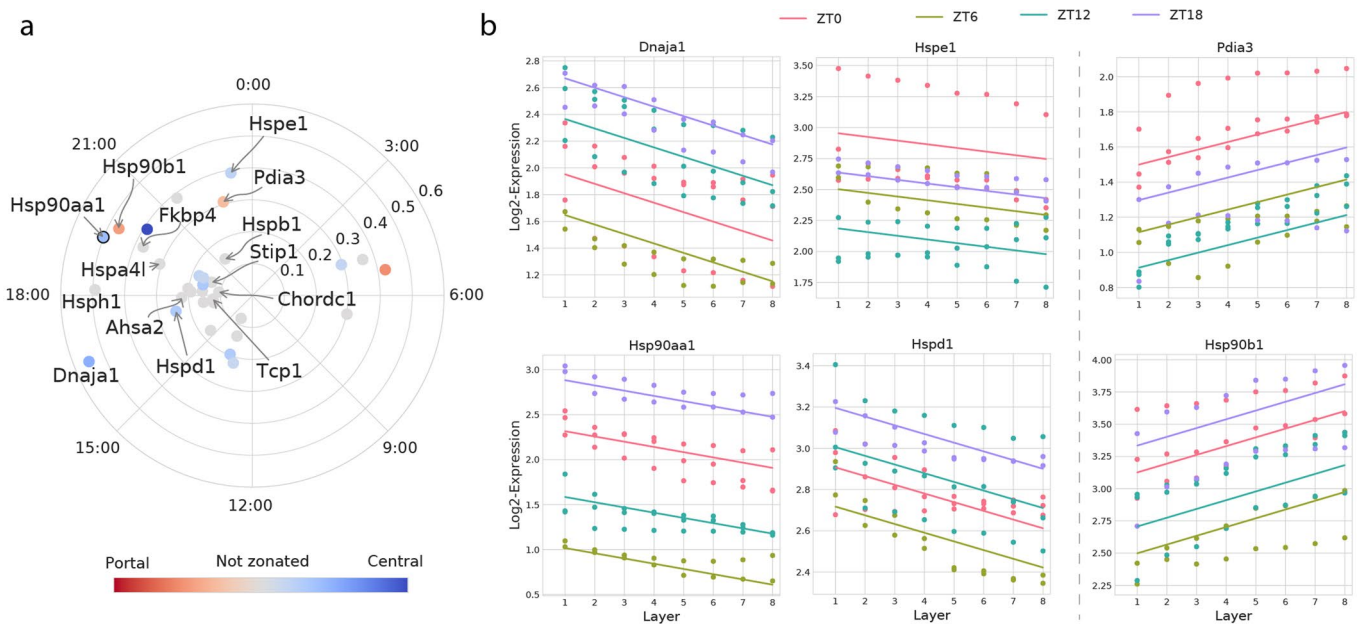

Extended Data Fig. 6 | Spatio-temporal mRNA expression profiles for heat-responsive genes. Represented genes correspond to the top 200 targets from the ChIP-Atlas list for mouse HSF1. a, Polar plot representation of the transcripts that are R, Z+R, or ZxR among the HSF1 targets from the ChIP-Atlas (http://chip-atlas.org/). Genes involved in chaperone functions (chaperones, co-chaperones, or chaperone facilitators) are named. Color indicates zonation, while grey dots show purely rhythmic genes. **b**, Spatial representation of the transcripts corresponding to proteins involved in chaperone functions, separated in central (left, cytoplasmic function) and portal (right, endoplasmic reticulum function) zonation.

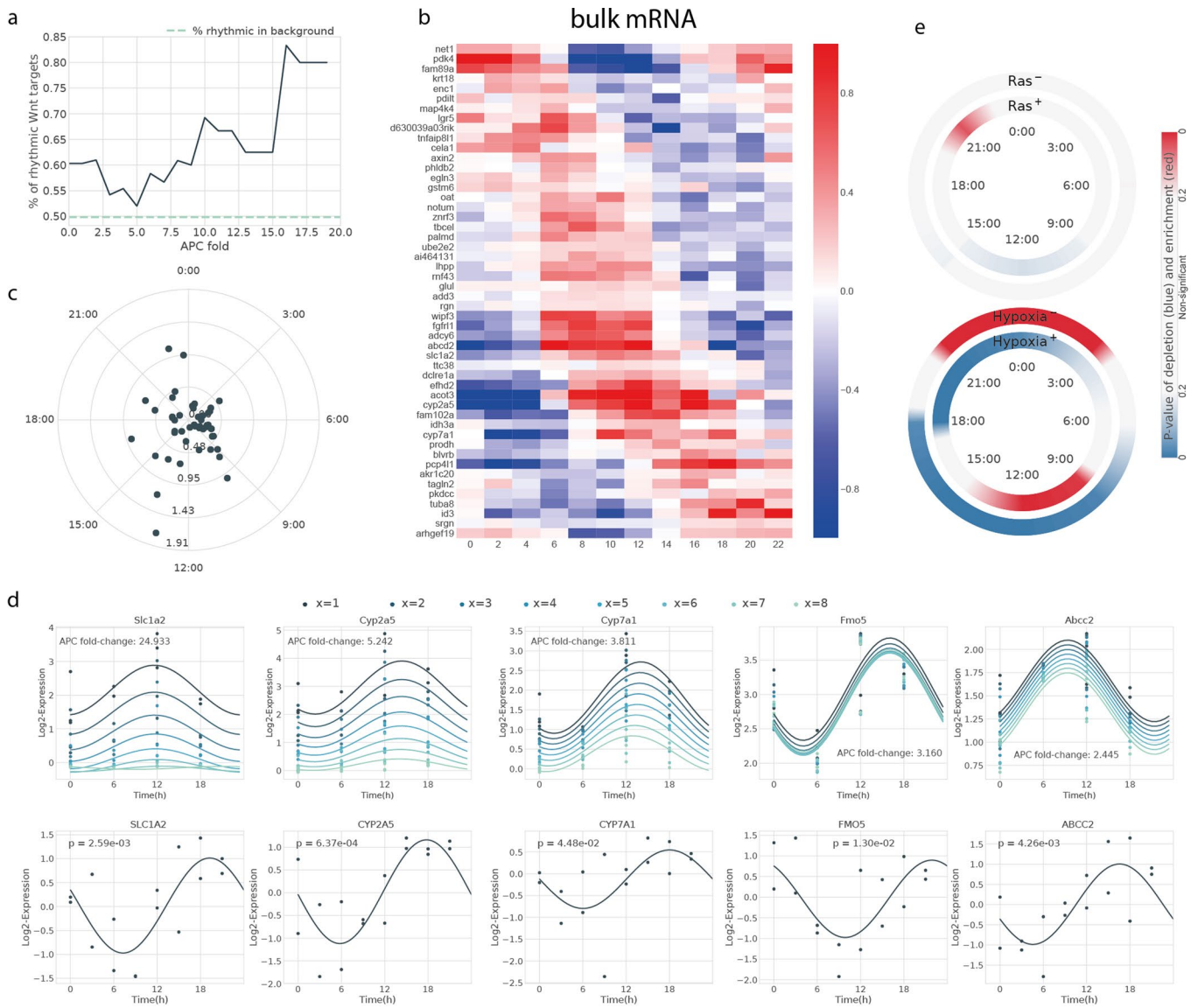

Extended Data Fig. 7 | Rhythmicity of Wnt targets in bulk RNA-seq, and proteomics liver time series data. a, Enrichment of rhythmic genes (R, Z+R and ZxR) among the targets of the Wnt pathway, computed on the bulk dataset (*Atger et al.*, [25]). Targets above a given percentile (x-axis) of Apc-KO fold change are considered. The percentage of rhythmic genes in the whole *Atger et al*. dataset is indicated by a dashed blue line. **b**, Bulk mRNA (coming from *Atger et al*. dataset) rhythmicity profiles of Wnt targets among the top-50 targets with highest Apc-KO fold change. Gene profiles are centered around their mean. An enrichment of the phases around ZT8-14 is observed, in agreement with Fig. 6a. **c**, Polar plot representation of the individual gene phases and amplitudes represented in panel b (bulk data). **d**, Temporal representation of selected genes profiles from the scRNA-seq (top, n=2 or n=3 animals depending on the time point, Methods) and bulk proteomics (bottom, data from *Robles et al.* [27], n=2 replicates per time point sampled every 3 h) data. Represented profiles are ones with (1) the highest Apc-KO fold change, (2) a significantly rhythmic protein ($p < 0.05$, standard harmonic regression, F-test), and (3) belonging to the Z+R or ZxR category. **e**, Enrichment/depletion at different times (window size: 3 h), of both positive and negative Ras (N=31 and N=33, respectively) and Hypoxia (N=73 and N=41, respectively) targets (background: all R and Z+R genes). Colormap shows p-values (two-tailed hypergeometric test): red (blue) indicates enrichment (depletion).

nature research

Corresponding author(s): Felix Naef, Shalev Itzkovitz

Last updated by author(s): Nov 3, 2020

Reporting Summary

Nature Research wishes to improve the reproducibility of the work that we publish. This form provides structure for consistency and transparency in reporting. For further information on Nature Research policies, see Authors & Referees and the Editorial Policy Checklist.

Statistics

For all statistical analyses, confirm that the following items are present in the figure legend, table legend, main text, or Methods section.

n/a	Confirmed
☐	☒ The exact sample size (*n*) for each experimental group/condition, given as a discrete number and unit of measurement
☐	☒ A statement on whether measurements were taken from distinct samples or whether the same sample was measured repeatedly
☐	☒ The statistical test(s) used AND whether they are one- or two-sided *Only common tests should be described solely by name; describe more complex techniques in the Methods section.*
☐	☒ A description of all covariates tested
☐	☒ A description of any assumptions or corrections, such as tests of normality and adjustment for multiple comparisons
☐	☒ A full description of the statistical parameters including central tendency (e.g. means) or other basic estimates (e.g. regression coefficient) AND variation (e.g. standard deviation) or associated estimates of uncertainty (e.g. confidence intervals)
☐	☒ For null hypothesis testing, the test statistic (e.g. *F*, *t*, *r*) with confidence intervals, effect sizes, degrees of freedom and *P* value noted *Give P values as exact values whenever suitable.*
☒	☐ For Bayesian analysis, information on the choice of priors and Markov chain Monte Carlo settings
☐	☒ For hierarchical and complex designs, identification of the appropriate level for tests and full reporting of outcomes
☐	☒ Estimates of effect sizes (e.g. Cohen's *d*, Pearson's *r*), indicating how they were calculated

Our web collection on statistics for biologists contains articles on many of the points above.

Software and code

Policy information about availability of computer code

Data collection	For RNA seq analysis, we used cellranger (3.1.0) mkfastq for demultiplexing of samples, and cellranger count for alignment and UMI count extraction. For smFISH we used MetaMorph software for microscope image acquisition.
Data analysis	R v3.4.2 using Seurat v2.1.0 was used for initial RNA-seq analyses. Data were analyzed using MATLAB R2019, R 3.5 and Python 3.7. Python packages used for analysis are "numpy v1.18", "scipy v1.5", "pandas v1.1.0", "statsmodel v0.12.0". The custom scripts developed to fit the mixed-effect models and to generate the main figures are available at https://c4science.ch/diffusion/10261/ and https://github.com/naef-lab/Circadian-zonation For smFISH quantification we used Matlab 2018b and FIJI win64. KEGG pathways analysis was done using the web-tool EnrichR(https://maayanlab.cloud/Enrichr/)

For manuscripts utilizing custom algorithms or software that are central to the research but not yet described in published literature, software must be made available to editors/reviewers. We strongly encourage code deposition in a community repository (e.g. GitHub). See the Nature Research guidelines for submitting code & software for further information.

Data

Policy information about availability of data

All manuscripts must include a data availability statement. This statement should provide the following information, where applicable:

- Accession codes, unique identifiers, or web links for publicly available datasets
- A list of figures that have associated raw data
- A description of any restrictions on data availability

All raw scRNA-seq data is deposited in GEO with accession code GSE145197.
The reconstructed spatio-temporal profiles are available at https://c4science.ch/diffusion/10261/ and https://github.com/naef-lab/Circadian-zonation

Field-specific reporting

Please select the one below that is the best fit for your research. If you are not sure, read the appropriate sections before making your selection.

☒ Life sciences ☐ Behavioural & social sciences ☐ Ecological, evolutionary & environmental sciences

For a reference copy of the document with all sections, see nature.com/documents/nr-reporting-summary-flat.pdf

Life sciences study design

All studies must disclose on these points even when the disclosure is negative.

Sample size	A total of 10 mice were used in scRNA-seq experiments. This was chosen to allow probing multiple times along the day (n=2,3 animals every 6h, see Methods). 8 animals (dt=3h) were used for the smFISH of strictly rhythmic genes (RNAScope), and 2 mice per time point for the smFISH of zonated-rhythmic genes (Stellaris). 8 animals (n=2 or n=3 per time point) were used for smFISH in endothelial cells.
Data exclusions	Some pre-filtering has been done both on the raw RNA-seq data and the rebuilt profiles. Details are carefully explained in the Methods section. criteria were not pre-established and were determined according to the quality of the data.
Replication	We have used n=2,3 biological replicate for each time point - all attempts at replication were successful as there was no sample which was excluded due to outliers.
Randomization	No allocation for experimental groups in our study.
Blinding	N/A - all mice were treated the same.

Reporting for specific materials, systems and methods

We require information from authors about some types of materials, experimental systems and methods used in many studies. Here, indicate whether each material, system or method listed is relevant to your study. If you are not sure if a list item applies to your research, read the appropriate section before selecting a response.

Materials & experimental systems

n/a	Involved in the study
☐	☒ Antibodies
☒	☐ Eukaryotic cell lines
☒	☐ Palaeontology
☐	☒ Animals and other organisms
☒	☐ Human research participants
☒	☐ Clinical data

Methods

n/a	Involved in the study
☒	☐ ChIP-seq
☒	☐ Flow cytometry
☒	☐ MRI-based neuroimaging

Antibodies

Antibodies used	Glutamine Synthetase (ab49873, Abcam, diluted 1:2000 in PBS/BSA 0.5%/Triton-X0.01%)
Validation	all antibodies were validated on manufacturer website.

Animals and other organisms

Policy information about studies involving animals; ARRIVE guidelines recommended for reporting animal research

Laboratory animals	8 -10 weeks old male mice (C57BL/6J) from Charles River (France) and 6 weeks old male mice (C57BL/6JOlaHsd), obtained from Envigo laboratories (Israel).
Wild animals	The study did not involve wild animals.
Field-collected samples	The study did not involve field collected samples.
Ethics oversight	All animal care and handling were approved by the Institutional Animal Care and Use Committee of Weizmann Institute of Science and by the Canton de Vaud laws for animal protection (authorization VD3197.b).

Note that full information on the approval of the study protocol must also be provided in the manuscript.